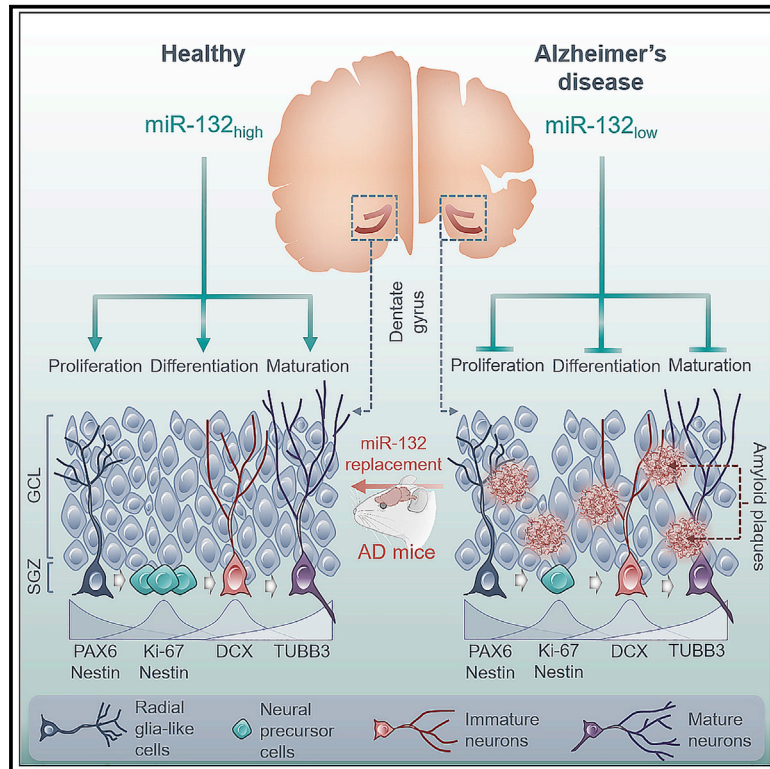


Restoring miR-132 expression rescues adult hippocampal neurogenesis and memory deficits in Alzheimer's disease

Graphical abstract



Authors

Hannah Walgrave, Sriram Balusu, Sarah Snoeck, ..., Carlo Sala Frigerio, Bart De Strooper, Evgenia Salta

Correspondence

b.strooper@ukdri.ucl.ac.uk (B.D.S.), e.salta@nin.knaw.nl (E.S.)

In brief

The process of generating new neurons from adult NSCs in the brain is hindered in AD. Walgrave et al. identify miR-132, a microRNA strongly downregulated in AD, as a potent regulator of neurogenesis in mouse and human, whose overexpression in adult NSCs rescues neurogenic and memory deficits in AD mice.

Highlights

- AD is associated with reduced miR-132 in the adult neurogenic niche and in human NSCs
- miR-132 regulates neurogenesis in adult mouse brain and human NSCs
- Increasing miR-132 in adult NSCs *in vivo* rescues neurogenic deficits in AD
- miR-132 supplementation alleviates memory deficits in AD

Article

Restoring miR-132 expression rescues adult hippocampal neurogenesis and memory deficits in Alzheimer's disease

Hannah Walgrave,^{1,2} Sriram Balusu,^{1,2} Sarah Snoeck,³ Elke Vanden Eynden,^{1,2} Katleen Craessaerts,^{1,2} Nicky Thrupp,^{1,2} Leen Wolfs,^{1,2} Katrien Horr , ^{1,2} Yannick Fourne,^{1,2} Alicja Ronisz,^{2,4} Edina Silajd i , ⁵ Amber Penning,³ Giorgia Tosoni,³ Zsuzsanna Callaerts-Vegh,^{2,6} Rudi D'Hooge,^{2,6} Dietmar Rudolf Thal,^{2,4} Henrik Zetterberg,^{7,8,9,10} Sandrine Thuret,⁵ Mark Fiers,^{1,2} Carlo Sala Frigerio,¹⁰ Bart De Strooper,^{1,2,10,*} and Evgenia Salta^{3,11,*}

¹VIB Center for Brain & Disease Research, 3000 Leuven, Belgium

²KU Leuven, Leuven Brain Institute, 3000 Leuven, Belgium

³Laboratory of Neurogenesis and Neurodegeneration, Netherlands Institute for Neuroscience, 1105BA Amsterdam, the Netherlands

⁴Laboratory for Neuropathology, KU Leuven, and Department of Pathology, UZ Leuven, 3000 Leuven, Belgium

⁵Institute of Psychiatry, Psychology & Neuroscience, King's College London, London, SE5 9RX, UK

⁶Laboratory for Biological Psychology, KU Leuven, 3000 Leuven, Belgium

⁷Clinical Neurochemistry Laboratory, Sahlgrenska University Hospital, 431 80 M lndal, Sweden

⁸Department of Neurodegenerative Disease, UCL Institute of Neurology, London, WC1N 3BG, UK

⁹Institute of Neuroscience and Physiology, Department of Psychiatry and Neurochemistry, Sahlgrenska Academy at the University of Gothenburg, 431 80 M lndal, Sweden

¹⁰UK Dementia Research Institute at UCL, London, WC1E 6BT, UK

¹¹Lead contact

*Correspondence: b.strooper@ukdri.ucl.ac.uk (B.D.S.), e.salta@nin.knaw.nl (E.S.)

<https://doi.org/10.1016/j.stem.2021.05.001>

SUMMARY

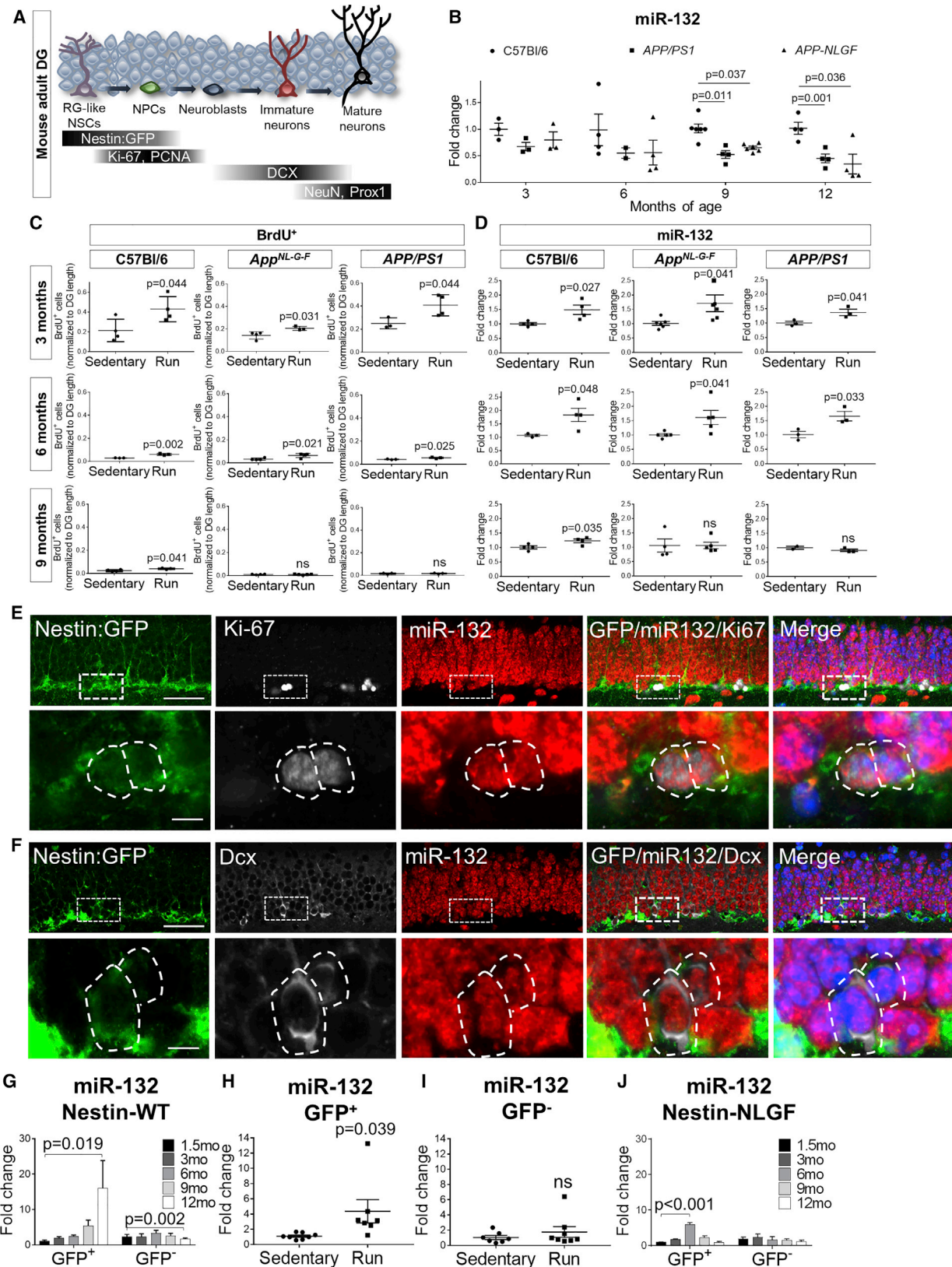
Neural stem cells residing in the hippocampal neurogenic niche sustain lifelong neurogenesis in the adult brain. Adult hippocampal neurogenesis (AHN) is functionally linked to mnemonic and cognitive plasticity in humans and rodents. In Alzheimer's disease (AD), the process of generating new neurons at the hippocampal neurogenic niche is impeded, yet the mechanisms involved are unknown. Here we identify miR-132, one of the most consistently downregulated microRNAs in AD, as a potent regulator of AHN, exerting cell-autonomous proneurogenic effects in adult neural stem cells and their progeny. Using distinct AD mouse models, cultured human primary and established neural stem cells, and human patient material, we demonstrate that AHN is directly affected by AD pathology. miR-132 replacement in adult mouse AD hippocampus restores AHN and relevant memory deficits. Our findings corroborate the significance of AHN in mouse models of AD and reveal the possible therapeutic potential of targeting miR-132 in neurodegeneration.

INTRODUCTION

Substantial evidence has demonstrated that neurogenesis occurs in adult human brain, is impaired in Alzheimer's disease (AD) patients, and could contribute to the memory decline observed in AD pathology (Boldrini et al., 2018; Cipriani et al., 2018; Gatt et al., 2019; Kempermann et al., 2018; Lucassen et al., 2020a, 2020b; Moreno-Jim nez et al., 2019; Mu and Gage, 2011; Tart et al., 2018; Tobin et al., 2019). Cumulative data implicate adult neurons born at the subgranular zone of the dentate gyrus in a wide range of physiological mnemonic processes, including episodic, declarative, contextual, and spatial memory, pattern separation, emotional control, functional forgetting, and cognitive flexibility (Anacker and Hen, 2017; Baptista and Andrade, 2018; Toda et al., 2019). Pattern separation, a memory function that enables separation of similar representations into distinct, non-overlapping memories, is causally linked to the process of adult hippocampal neurogenesis (AHN) and is functionally dependent

on the adult-born neurons in the rodent dentate gyrus (Clelland et al., 2009; Danielson et al., 2016; Sahay et al., 2011). Several studies have reported impaired performance in pattern separation tasks in patients with amnesic mild cognitive impairment (MCI) with increased rate of progression to clinically probable AD (Petersen et al., 2001) and also in late-stage AD patients (Ally et al., 2013; Wesnes et al., 2014; Yassa et al., 2010). Interestingly, larger numbers of neuroblasts in the dentate gyrus correlate with better ante-mortem cognitive status in MCI patients (Tobin et al., 2019), while proliferation and differentiation capacity of adult neural stem cells (NSCs) have been also correlated with memory performance in epilepsy patients (Coras et al., 2010).

A deeper understanding of the molecular mechanisms involved in AHN becomes particularly relevant when considering AHN as a therapeutic target for neurodegenerative diseases such as AD. Previously, we have shown that miR-132 regulates the timing for cell cycle exit of radial glia-like (RGL) NSCs in the developing vertebrate spinal cord (Salta et al., 2014). Much



(legend on next page)

less is known about the role of miR-132 in adult rodent and human dentate gyrus, yet miR-132 expression is low in nestin-positive NSCs and progenitors and gradually increases during the process of neuronal differentiation (Luikart et al., 2011). Moreover, miR-132 deletion in adult dentate gyrus induces significant alterations in neurite maturation, spine formation, and synaptic activity of newborn neurons, which compromises their functional integration into the adult hippocampal circuitry (Luikart et al., 2011; Magill et al., 2010). Interestingly, intersectional analysis of hippocampal transcriptomic profiles in miR-132-overexpressing and miR-132 conditional knockout mice reveals strong effects on genes involved in neurogenesis and cell proliferation (Hansen et al., 2016). Although there is no conclusive proof, these data suggest a possible role for miR-132 in adult neurogenesis under physiological conditions. Intriguingly, miR-132 is strongly and reproducibly downregulated in the hippocampus of human AD patients (Hébert et al., 2013; Lau et al., 2013; Patrick et al., 2017; Pichler et al., 2017; Salta and De Strooper, 2017; Salta et al., 2016; Smith et al., 2015; Wong et al., 2013; Zhu et al., 2016). miR-132 overexpression in primary neurons or mouse brain represses pathological hallmarks of AD, such as amyloid plaques, TAU hyperphosphorylation and deposition, and neuronal death (El Fatimy et al., 2018; Hernandez-Rapp et al., 2015; Salta et al., 2016; Smith et al., 2015; Wang et al., 2017; Wong et al., 2013; Zhu et al., 2016; reviewed in Salta and De Strooper, 2017). However, the role of miR-132 in AHN in the context of AD remains elusive. Here, we report that miR-132 regulation is an integral and indispensable part of AHN and that miR-132 replacement restores AHN and memory deficits in two distinct mouse models of AD by exerting diverse effects at the adult hippocampal neurogenic niche.

RESULTS

AHN aberrations in AD parallel miR-132 deficiency in the dentate gyrus

In the subgranular zone, adult radial glia (RG)-like quiescent NSCs follow a stereotypical neurogenic trajectory to eventually

give rise to dentate granule neurons (Bond et al., 2015). Each of these activation and differentiation cellular states can be labeled with distinct markers (Figure 1A).

To obtain an independent proof of concept of AHN deficiency in AD, we first performed a postmortem human brain immunohistochemical analysis of proliferating neuronal progenitors at the subgranular zone of the dentate gyrus in tissue sections from ten non-demented control individuals and ten AD patients (Figure S1A). Normalized proliferating cell nuclear antigen (PCNA)⁺ cell counts were significantly decreased by approximately 50% in AD dentate gyrus (Figure S1B). Astrocytes were negative for PCNA (Figures S1C and S1D), while PCNA⁺ microglia were excluded on the basis of their larger and less spherical shape compared with PCNA⁺ neuronal precursor cells (Figures S1E and S1F). This reduction in the pool of proliferating cells, which eventually give rise to adult-born neurons, aligns with recent reports that provide strong evidence for decreased AHN in AD (Moreno-Jiménez et al., 2019; Tobin et al., 2019). Hence, miR-132 deficiency in the hippocampus of AD patients (Hébert et al., 2013; Lau et al., 2013; Patrick et al., 2017; Pichler et al., 2017; Salta and De Strooper, 2017; Salta et al., 2016; Smith et al., 2015; Wong et al., 2013; Zhu et al., 2016) parallels the decreased proliferation of neuronal precursors in the dentate gyrus.

We then asked whether miR-132 deficiency in AD is also functionally associated with the adult neurogenic niche. To address a possible genotype bias, we used two AD models, one overexpressing mutated forms of the human amyloid precursor protein (APP) and presenilin 1 (PS1) (*APP/PS1*) (Radde et al., 2006), and one carrying a knockin mutated humanized *App* gene (*App^{NL-G-F}*) (Saito et al., 2014). miR-132 levels were measured at different ages in the dentate gyrus of wild-type and AD mice using real-time PCR (Figure 1B). We observed an early trend for miR-132 downregulation in AD dentate gyrus compared with wild-type, which became significant at 9 months in both the *APP/PS1* and the *App^{NL-G-F}* animals. Similar changes were observed in female mice (Figure S1G). As synaptic loss in the hippocampus might be a confounding variable contributing to the reduction of synaptic

Figure 1. Adult neurogenesis is impaired by AD pathology and is associated with miR-132 levels in the adult hippocampal neurogenic niche

(A) Schematic representation of the main fate transitions during adult hippocampal neurogenesis in the dentate gyrus (DG), including radial glia (RG)-like neural stem cells (NSCs), neuronal precursor cells (NPCs), neuroblasts, and immature and mature neurons, as indicated by the expression pattern of distinct molecular markers.

(B) Semiquantitative real-time PCR of miR-132 levels in the dentate gyrus of C57BL/6, *APP/PS1*, and *App^{NL-G-F}* mice at 3, 6, 9, and 12 months of age. n = 3–6 mice per time point.

(C) BrdU⁺ cells in the subgranular zone of the dentate gyrus in C57BL/6, *APP/PS1*, and *App^{NL-G-F}* control (sedentary) mice or mice exposed to voluntary running for 1 month (run) at 3, 6, and 9 months of age. n = 4–6 mice per group.

(D) Semiquantitative real-time PCR of miR-132 levels in the dentate gyrus of C57BL/6, *APP/PS1*, and *App^{NL-G-F}* sedentary control or running mice at 3, 6, and 9 months of age. n = 4–6 mice per group.

(E and F) miR-132 *in situ* hybridization coupled to GFP and Ki-67 (E) or GFP and doublecortin (DCX) (F) immunolabeling in the dentate gyrus of 3-month-old Nestin:GFP mice. Lower panels show magnified views of the cells in the regions indicated by dashed rectangles in upper panels. Dashed outlines in lower panels indicate cellular margins. "Merge" indicates images obtained from overlaying images separately acquired with distinct channels (blue is DAPI). Scale bars, 50 μ m (upper panels) and 10 μ m (lower panels).

(G) Semiquantitative real-time PCR of miR-132 levels in GFP⁺ or GFP⁻ populations isolated using FACS from the dentate gyrus of Nestin:GFP mice at 1.5, 3, 6, 9, and 12 months of age. n = 6–8 mice per time point.

(H and I) Semiquantitative real-time PCR of miR-132 levels in GFP⁺ (H) or GFP⁻ (I) populations sorted from the dentate gyrus of sedentary control or running Nestin:GFP mice at 3 months of age. n = 6–8 mice per group.

(J) Semiquantitative real-time PCR of miR-132 levels in GFP⁺ or GFP⁻ populations sorted from the dentate gyrus of Nestin-NLGF mice at 1.5, 3, 6, 9, and 12 months of age. n = 3–5 mice per time point.

Values are presented as mean \pm SEM. In (B), (G), and (J), two-way ANOVA with Tukey's post hoc test for multiple comparisons was used, while in (C), (D), (H), and (I), Student's t test was used. See also Figures S1–S3 and Table S1.

miR-132 levels (Edbauer et al., 2010), we assessed the expression levels of syntaxin 1A (*Stx1A*) and synaptophysin (*Syp*) as a proxy for synaptic integrity using real-time PCR (Dickey et al., 2003). No changes in the levels of these transcripts were observed at 12 months of age in wild-type or AD mouse dentate gyrus (Figure S1H). To dissect more subtle synaptic alterations, we analyzed co-localizing presynaptic (VGlut1-positive) and postsynaptic (PSD95-positive) puncta in the granular cell layer, the molecular cell layer, and the hilar area at 3 and 9 months of age. Only a modest decrease of synaptic puncta was observed in 9-month-old *APP/PS1* and *App^{NL-G-F}* dentate gyrus compared with age-matched wild-type animals (Figures S1I–S1K), suggesting that the robust miR-132 decline in old AD dentate gyrus is not primarily induced by synaptic loss.

We next investigated whether AHN is affected in the two AD mouse models. We used incorporation of a synthetic analog of thymidine, bromodeoxyuridine (BrdU), in the DNA of cells undergoing mitosis, in mice exposed to voluntary running, which is a widely used paradigm for induction of neuronal progenitor proliferation and adult neurogenesis (van Praag et al., 1999). One month of voluntary running increased the number of proliferating neuronal precursor cells at the subgranular zone of the dentate gyrus of both wild-type and AD mice compared with sedentary controls at 3 and 6 months of age (Figures 1C and S2). However, the potential to induce neuronal progenitor proliferation at the subgranular zone upon running was compromised in 9-month-old AD dentate gyrus, as opposed to wild-type mice (Figures 1C and S2). Notably, this was paralleled by changes in miR-132 expression in the dentate gyrus. miR-132 levels significantly increased in running mice of all three genotypes at 3 and 6 months, yet no change was observed in running AD mice at 9 months of age (Figure 1D). miR-212, a cognate microRNA of miR-132 which is co-transcribed from the same genetic locus, did not potently respond to physical exercise at any of the assessed time points in any of the genotypes (Figure S1L).

Taken together, these results point toward a possible correlation between an amyloid plaque or amyloid beta (A β) oligomer pathology-induced effect on miR-132 expression and compromised AHN in two different mouse models for amyloid plaque pathology in AD.

miR-132 expression at the adult hippocampal neurogenic niche is affected by A β pathology

We next assessed miR-132 localization in the adult neurogenic niche. We employed a nestin promoter-based green fluorescent protein (Nestin:GFP) reporter line in conjunction with additional markers to label NSCs and neuronal precursors at the subgranular zone of the dentate gyrus (Mignone et al., 2004) and used fluorescence *in situ* hybridization and fluorescence-activated cell sorting (FACS) to determine the expression of miR-132. We use the term “Nestin:GFP⁺ niche cells” to collectively refer to the GFP-positive dentate gyrus populations (Artegiani et al., 2017; Shin et al., 2015). Fluorescence *in situ* hybridization revealed that at basal conditions miR-132 is expressed in Nestin:GFP⁺/Ki-67⁺ proliferating neuronal precursor cells (Figure 1E) and Nestin:GFP⁺/DCX⁺ immature neurons (Figure 1F) at the subgranular zone. Hybridization with a scrambled probe was used as a negative control (Figures S3A and S3B). Using a more quantitative method, we next confirmed detection using

real-time PCR and assessed the time course of miR-132 expression in Nestin:GFP⁺ niche cells isolated from wild-type mouse dentate gyrus. miR-132 levels were already detectable in Nestin:GFP⁺ and to a smaller extent in Nestin:GFP⁺ populations at 1.5 months of age (Figure 1G). We observed a significant and specific increase of miR-132 expression in sorted cells at 12 months (Figures 1G and S3C). Interestingly, miR-132 upregulation did not occur in the Nestin:GFP⁺ fraction which consists mainly of granule dentate neurons (Figure 1G), indicating that miR-132 is upregulated in the neurogenic niche, but not in the mature neurons, over time. Moreover, induction of adult neurogenesis via physical exercise elicited a significant upregulation of miR-132 only in the Nestin:GFP⁺ niche cell fraction (Figure 1H) and not in the Nestin:GFP⁺ neuronal population (Figure 1I). This upregulation was specific for miR-132, as the levels of miR-212 and of miR-124, a brain-enriched microRNA, were not changed (Figures S3D–S3G). We then asked whether amyloid plaque pathology affects miR-132 levels at the hippocampal neurogenic niche. To address this question, we crossed Nestin:GFP with *App^{NL-G-F}* (Nestin-NLGF) mice and measured miR-132 levels in GFP⁺ and GFP⁺ cells isolated from the dentate gyrus at different ages. miR-132 levels in the Nestin:GFP⁺ niche cells of the AD mouse dentate gyrus increased at 6 months of age, similarly to wild-type mice, but sharply decreased at 9 months (Figures 1J and S3I), coinciding with the inability of the neuronal progenitors in the AD mouse model brain to proliferate upon running. No significant changes were observed for miR-212 (Figure S3H). Taken together, these data show that miR-132 is recruited by adult NSCs and progenitors as part of the response to exercise- or aging-related stimuli but fails to do so upon exposure to A β pathology in the hippocampal neurogenic niche.

miR-132 is required for proliferation of neural precursors and neuronal differentiation in adult dentate gyrus

We then asked whether miR-132 is required for adult neurogenesis in wild-type dentate gyrus. As expected, voluntary running induced an increase in the numbers of BrdU⁺ and Ki-67⁺ proliferating neuronal precursors, Nestin:GFP⁺ NSCs and progenitors and DCX⁺ immature neurons at the subgranular zone of the dentate gyrus in scramble control-injected wild-type mice compared with sedentary animals (Figures 2A–2F). However, the effect of physical exercise on AHN was abrogated by miR-132 knockdown (Figure S4A) in running mice intracerebroventricularly (i.c.v.) injected with an antisense oligonucleotide against miR-132 (AntagomiR-132 [Ant-132]) (Figures 2A–2F), demonstrating that miR-132 is required for the induction of AHN by running. miR-132 knockdown was confirmed in both the Nestin:GFP⁺ and the Nestin:GFP⁺ fractions of the neurogenic niche (Figure S4B) and was specific to miR-132 (Figure S4C). Immunostaining against the proliferation marker PCNA confirmed that miR-132 knockdown abolishes the positive effect of running on neuronal precursor proliferation (Figures S4D and S4E). As miR-132 is also involved in the regulation of neuronal apoptosis (Wong et al., 2013), we asked whether the net effect of miR-132 knockdown could be mediated by interfering with the physiological process of neuronal progenitor elimination by apoptotic death. Quantification of the cells labeled by an antibody against cleaved caspase-3, a marker of apoptosis, did not reveal any

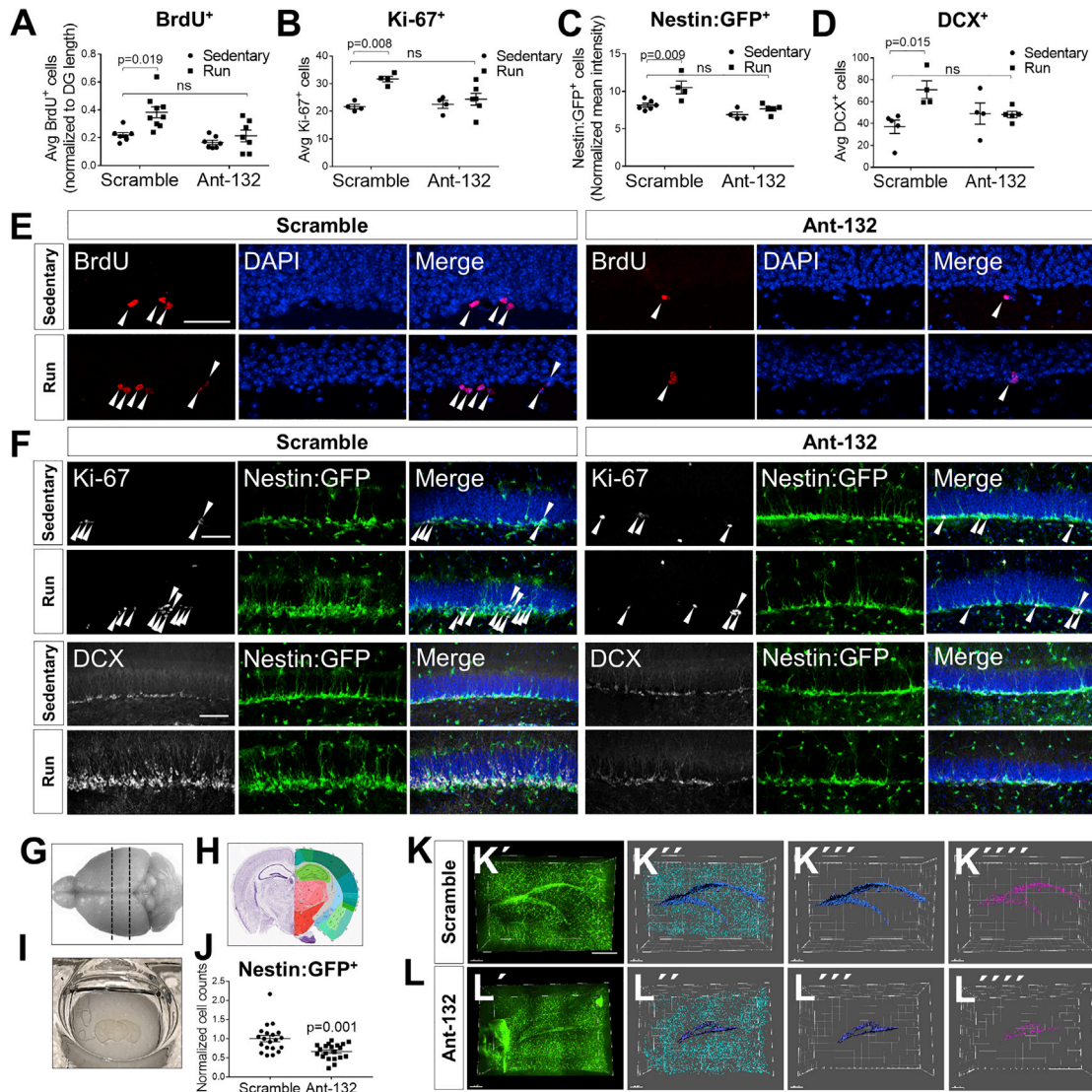


Figure 2. miR-132 is required for adult neurogenesis

(A) Quantification of BrdU⁺ cells in the dentate gyrus of control- or AntagomiR-132 (Ant-132)-injected, sedentary or running C57BL/6 mice at 9 months of age. $n = 6-9$ mice per group.

(B-D) Quantification of Ki-67⁺ (B), Nestin:GFP⁺ (C), and DCX⁺ cells (D) in the dentate gyrus of control- or Ant-132-injected, sedentary or running Nestin:GFP mice at 3 months of age. $n = 4-6$ mice per group.

(E) BrdU⁺ proliferating neuronal progenitors in the dentate gyrus of scramble- or Ant-132-injected, sedentary or running C57BL/6 mice at 9 months of age. Arrowheads indicate BrdU⁺ cells. "Merge" indicates images obtained from overlaying images separately acquired with distinct channels. Scale bars, 50 μ m.

(F) Ki-67⁺ proliferating progenitors and DCX⁺ immature neurons in control- or Ant-132-injected, sedentary or running Nestin:GFP mice at 3 months of age. Arrowheads indicate Ki-67⁺ amplifying progenitors. "Merge" indicates images obtained from overlaying images separately acquired with distinct channels (blue is DAPI). Scale bars, 50 μ m.

(G) Schematic of mouse brain indicating the area of sectioning (dashed lines) used for tissue clearing.

(H) Coronal mouse brain section at P56, position 293, showing hippocampal structure. Image adapted from Allen Brain Atlas (http://mouse.brain-map.org/experiment/thumbnails/100048576?image_type=atlas).

(I) Cleared coronal brain section.

(J) Quantification of GFP⁺ cells in the subgranular layer of the dentate gyrus in running scramble- or Ant-132-injected 3-month-old Nestin:GFP mice. $n = 10$ mice per group; two hemispheric dentate gyri per mouse.

(K and L) Three-dimensional (3D) reconstruction and image processing for whole-mount GFP⁺ cell counting in scramble-injected (K) or Ant-132-injected (L) mice upon running. Green, GFP⁺ cells; dark blue, reconstructed dentate gyrus surface; purple, GFP⁺ cells lining the dentate gyrus used for quantification; light blue, GFP⁺ cells away from dentate gyrus. Scale bar, 300 μ m.

Values are presented as mean \pm SEM. Two-way ANOVA with Tukey's post hoc test for multiple comparisons was used in (A)-(D) and Student's t test in (J). See also Figure S4.

significant changes between groups (Figures S4F and S4G), indicating that miR-132 regulation of AHN is not effectuated at the level of apoptotic control. Interestingly, miR-132 deficiency also impaired the exercise-induced elevation of brain-derived neurotrophic factor (*Bdnf*) (Figure S4H), which has recently emerged as an essential neurotrophin for the fitness of the adult hippocampal neurogenic niche and the cognitive recovery in an AD mouse model (Choi et al., 2018).

To obtain a measurement of the global effect of miR-132 deficiency on the NSCs and progenitors *in vivo*, we used tissue clearing to assess the numbers of the Nestin:GFP⁺ cells at the subgranular zone of the whole dentate gyrus (Figures 2G–2I). We compared the numbers of Nestin:GFP⁺ NSCs and progenitors at the subgranular zone of running mice (Figures 2J–2L) injected either with scramble control (Video S1) or with Ant-132 (Video S2). miR-132 knockdown resulted in a small but significant decrease in the total number of NSCs and progenitors (Figure 2J), confirming our previous observations. Together, these data unequivocally demonstrate that miR-132 is required for the induction of neurogenesis in the dentate gyrus *in vivo*.

miR-132 regulates neuronal differentiation and is downregulated by AD-related pathology in human NSCs

We next assessed whether miR-132 regulation is also involved in the differentiation of human neuronal precursor to neurons. miR-132 levels significantly increased by 20-fold upon neural induction of primary human embryonic stem cells to neuronal precursors and were further boosted by more than 300-fold during neuronal maturation (Figures 3A and 3B). miR-212 levels, in contrast, were only subtly altered over the course of neuronal differentiation and maturation (Figure S5A). The progression of neuronal differentiation was monitored by measuring beta tubulin 3 (TUBB3) mRNA levels (Figure 3C).

A similar upregulation of miR-132 was detected in an immortalized human NSC and progenitor line of mesencephalic origin (RenCells VM) upon induction of neuronal differentiation (Figures 3D and 3E), providing further support for the functional significance of miR-132 in the process of human neurogenesis. The differentiation efficiency was monitored by immunostaining for NESTIN and SOX2 (NSCs), Ki-67 (proliferating neuronal precursor cells), and TUBB3 (mature neurons) (Figures S5B and S5C). The levels of TUBB3 were additionally measured using semiquantitative real-time PCR (Figure 3E). Notably, miR-132 transfection in human undifferentiated RenCell NSCs and progenitors (Figures S5D and S5E) resulted in a significant upregulation of TUBB3 (Figures 3F and S5J), suggesting that miR-132 is a positive regulator of neurogenesis in human neuronal progenitors. A 10-times-lower miR-132 dose (Figure S5F) had an overall milder yet still significant effect on the levels of TUBB3 (Figure S5G). Conversely, miR-132 knockdown in differentiating RenCell NSCs and progenitors (Figures S5H and S5I) induced a decrease of TUBB3 levels (Figures 3G and S5K). Similar results were obtained upon miR-132 overexpression (Figures 3H and 3I) and knockdown (Figure 3J) in human neural precursor cells of hippocampal origin (HPC0A07/03C), corroborating the relevance of miR-132 regulation over human neurogenesis.

To explore whether A β pathology can prompt miR-132 downregulation in human neural stem and progenitor cells, we treated human embryonic stem cell-derived neuronal precursor cells with

A β _{1–42} oligomers. Incubation of these cells with 5 μ M A β _{1–42} for 72 h affected their proliferation capacity (Figure 3K) and induced a specific miR-132 decrease compared with cells incubated with a scramble control (Figures 3K and S5L). The hippocampal neurogenic niche is highly vascularized and hence permissive to molecular cues transmitted via communication with the systemic environment (Villeda et al., 2011). Previously, it was shown that incubation of human neuronal precursor cells of hippocampal origin with serum samples derived from AD patients compared with non-demented control individuals reduced cell proliferation (Maruszak et al., 2017). We extend this observation here by demonstrating that neuronal precursor cells treated with sera derived from AD patients showed significantly reduced miR-132, but not miR-212, levels (Figures 3L and S5M), while incubation with the AD sera also affected cell proliferation (Figure 3L). These data confirm that miR-132 expression is suppressed in human stem cells by A β oligomers or other AD-related serum-derived factors.

miR-132 alleviates proliferation and differentiation deficits of adult neural precursors in AD mouse model brain

We next investigated whether boosting miR-132 levels could ameliorate the AHN deficits we observed in the two AD mouse models. Control-injected 9-month-old *APP/PS1* mice were not able to induce AHN upon running, as assessed by the numbers of BrdU⁺ and Ki-67⁺ proliferating neuronal precursor cells and DCX⁺ immature neurons at the subgranular zone of the dentate gyrus (Figures 4A–4D). However, upon miR-132 overexpression via i.c.v. injection of a synthetic miR-132 mimic oligonucleotide (Figure S6A), we observed significant increases in these cell populations under sedentary conditions. Similar results were obtained in the *App*^{NL-G-F} male (Figures 4E–4H and S6B) and *App*^{NL-G-F} female mice (Figures S6C and S6D), suggesting that this was not a strain- or gender-dependent effect. To assess whether the apparent increase in proliferating progenitors and immature neurons is the result of an intrinsic transcriptional response of the resident niche cells to miR-132 and to account for the variation in cell numbers between miR-132-overexpressing and control animals, we measured the levels of markers of stemness (*Pax6*), cell proliferation (*Mki67*), and early neuronal fate (*Dcx*) in equal numbers of sorted Nestin:GFP⁺ cells isolated from the dentate gyrus of miR-132- or control-injected mice (Figures 4I and S7A). miR-132 overexpression significantly repressed early stem cell identity in this pool of cells and induced transcriptomic changes indicative of increased proliferation and differentiation rates.

Cell-autonomous regulatory effects of miR-132 in adult NSCs and progenitors at the AD mouse hippocampal niche

Considering that i.c.v. infusion of miR-132 mimic oligonucleotides may exert broad effects in different cell types at the adult hippocampal niche, we deployed two distinct strategies to overexpress miR-132 specifically in adult NSCs and their progeny in the dentate gyrus of 9-month-old *App*^{NL-G-F} mice (Figure 5A).

First, a lentiviral vector (LV PGK:mCHERRY) expressing an mCHERRY reporter and a miR-132-overexpressing hairpin under the control of the PGK promoter (Suh et al., 2018) was

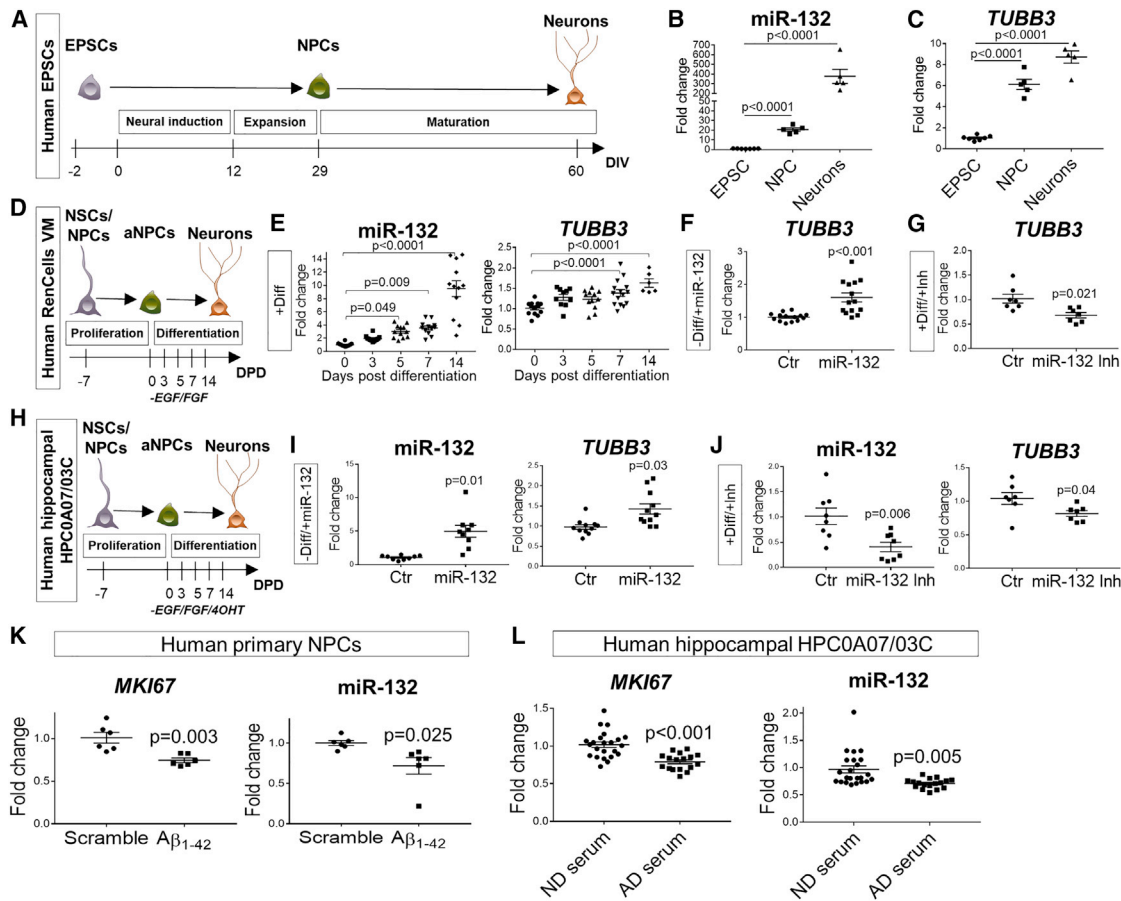


Figure 3. miR-132 regulatory effects in human neural stem cells

(A) Schematic representation of the protocol used for neural induction of human embryonic pluripotent stem cells (EPSCs). DIV, days *in vitro*. (B and C) Semiquantitative real-time PCR of miR-132 (B) and tubulin (*TUBB3*) (C) levels in EPSCs (day -2), NPCs (day 29), and mature neurons (day 60). $n = 3$ independent experiments. (D) Schematic diagram of the protocol used for neural differentiation of cultured immortalized human mesencephalic neuronal progenitors. NSC, neural stem cell; NPC, neuronal progenitor cell; aNPC, amplifying neuronal progenitor cell; DPD, days post-differentiation. (E) Semiquantitative real-time PCR of miR-132 and *TUBB3* upon induction of differentiation (Diff) in human neuronal progenitors. $n = 3$ independent experiments. (F and G) Semiquantitative real-time PCR of *TUBB3* following miR-132 overexpression (miR-132) without induction of differentiation (F) or miR-132 knockdown (miR-132 Inh) upon induction of differentiation at 3 days post-differentiation (G). $n = 3$ independent experiments per condition. (H) Schematic diagram of the protocol used for neural differentiation of cultured immortalized human hippocampal neuronal progenitors. (I and J) Semiquantitative real-time PCR of miR-132 and *TUBB3* following miR-132 overexpression (miR-132) without induction of differentiation (I) or miR-132 knockdown (miR-132 Inh) upon induction of differentiation at 3 days post-differentiation (J). $n = 3$ independent experiments per condition. (K and L) Semiquantitative real-time PCR of the proliferation marker *MKI67* (coding for Ki-67) and miR-132 in embryonic pluripotent stem cell-derived primary human neuronal precursor cells (NPCs) (K) or an established human hippocampal neural precursor (hNPC) line (HPC0A07/03C) (L) upon treatment with $A\beta_{1-42}$ oligomers and a scramble control peptide (K) or incubation in AD and control serum (L). $n = 6$ biological replicates in (K); 23 (ND) and 17 (AD) in (L). Values are presented as mean \pm SEM. For data analysis, one-way ANOVA with Tukey's post hoc test for multiple comparisons was applied in (B), (C), and (E), while Student's *t* test was used in (F), (G), and (I)–(L). See also [Figure S5](#) and [Table S4](#).

used for stereotactic injections into the dentate gyrus ([Figure 5B](#)). Considering the possibility that LV PGK:mCherry, apart from adult NSCs, may also transduce a proportion of developmentally born granule cells, we additionally used a retroviral approach (RV CAG:GFP) ([Zhao et al., 2006](#)) to target miR-132 overexpression to proliferating adult neuronal precursors in a second mouse cohort ([Figure 5C](#)).

We analyzed dendritic development in 4-week-old neurons, a time point at which these cells are functionally integrated ([van Praag et al., 2002](#); [Zhao et al., 2006](#)). Consistent with the AHN deficits observed earlier, no running-induced effects were

observed in the dendritic length and arbor complexity of labeled granule cells in *App^{NL-G-F}* mice injected with either the lentiviral or the retroviral control vectors 4 weeks post-injection ([Figures 5D–5G](#)). However, both lentiviral and retroviral miR-132 overexpression reversed these deficits in the neuronal progeny under both sedentary and running conditions ([Figures 5D–5G](#)).

At 4 weeks of age, newly born neurons already receive excitatory input from the perforant path, which connects the dentate gyrus to the entorhinal cortex ([van Praag et al., 2002](#)). Both lentiviral and retroviral miR-132 overexpression in *App^{NL-G-F}* granule cells 4 weeks post-injection significantly increased spine

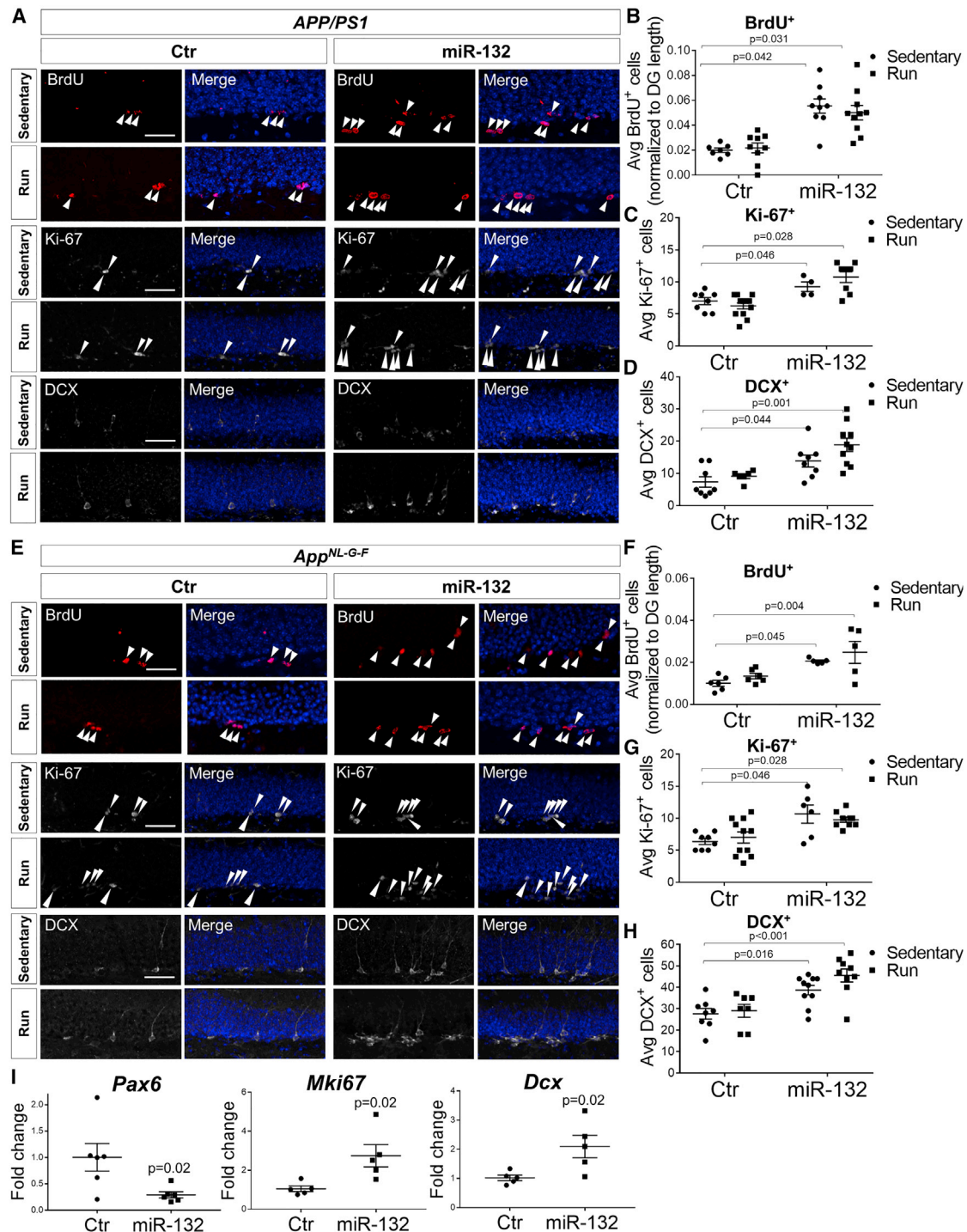


Figure 4. miR-132 overexpression ameliorates adult neurogenesis deficits in AD mouse hippocampus

(A) Immunolabeling of BrdU⁺, Ki-67⁺, and DCX⁺ cells in the dentate gyrus of control (Ctr)- or miR-132-injected, sedentary or running *APP/PS1* mice at 9 months of age. “Merge” indicates images obtained from overlaying images separately acquired with distinct channels (blue is DAPI). Scale bar, 50 μ m. Arrowheads indicate positively labeled cells.

(B–D) Quantification of BrdU⁺ (B), Ki-67⁺ (C), and DCX⁺ cells (D) in the dentate gyrus of control (Ctr)- or miR-132-injected, sedentary or running *APP/PS1* mice at 9 months of age. n = 6–10 mice per group.

(E) Immunolabeling of BrdU⁺, Ki-67⁺, and DCX⁺ cells in the dentate gyrus of control (Ctr)- or miR-132-injected, sedentary or running *App^{NL-G-F}* mice at 9 months of age. “Merge” indicates images obtained from overlaying images separately acquired with distinct channels (blue is DAPI). Scale bar, 50 μ m. Arrowheads indicate positively labeled cells.

(legend continued on next page)

density, as opposed to running, which had no effect (Figures 5H–5K).

Together, these data suggest that miR-132 regulates late-stage neuronal maturation in a cell-autonomous manner, and that increasing miR-132 in adult NSCs and progenitors can ameliorate deficits in the dentate gyrus of an AD mouse model.

miR-132 promotes AHN by modulating a complex molecular network in adult NSCs

In order to identify the mechanisms underpinning the positive regulatory effect of miR-132 in AHN, we used a single-cell RNA sequencing approach to assess miR-132-specific transcriptional responses in the Nestin:GFP-labeled resident niche cells (Figure 6A). Nestin:GFP⁺ niche cells were isolated from dentate gyri of mice that were i.c.v. injected with either miR-132 mimic or control oligonucleotides, and single-cell libraries were prepared as discussed in STAR Methods. The extent and specificity of miR-132 overexpression was assessed in Nestin:GFP⁺ and Nestin:GFP⁻ bulk-sorted cells (Figure S7A). Although miR-132 levels were, as expected, elevated in both populations compared with control-injected animals, the increase was significant only in the Nestin:GFP⁺ fraction (Figure S7A), which may reflect the relative high baseline expression of miR-132 in the neuronal fraction of the dentate gyrus. A total of 709 Nestin:GFP⁺ single niche cells were sequenced using the Smart-seq2 protocol. Unsupervised hierarchical clustering of the dataset using the Seurat algorithm revealed 7 populations, which were projected on a t-distributed stochastic neighbor embedding (t-SNE) map for visualization (Figure 6B). On the basis of the expression levels of well-characterized marker genes (Artegiani et al., 2017; Hochgerner et al., 2018; Zeisel et al., 2018; Table S5, Literature-Markers), we defined cluster identity (Figures 6B and S7B; Table S5, ModuleScore), mapping the subpopulations as RGL NSCs, neuronal intermediate precursor cells (NPCs), astrocytes, oligodendrocyte precursor cells (OPCs), myelin-forming oligodendrocytes (MFOLs), endothelial cells, and pericytes. Cell-type-enriched genes were identified by comparing each cell type cluster with all others (Figure S7C; Table S5, Cluster-Markers). The distribution of cells across clusters was not altered in a statistically significant way upon miR-132 overexpression in these experiments (data not shown).

Differential gene expression analysis between miR-132-overexpressing and control cells within each cluster did not reveal any significantly deregulated transcripts after correction for multiple testing comparisons (Table S6), an observation that could be indicative of the frequently documented limited effect sizes of microRNA regulation (Moore et al., 2015). As microRNAs may elicit changes on cellular dynamics via widespread yet subtle effects on the transcriptome (Liufu et al., 2017), we next assessed the possible impact of miR-132 overexpression on molecular pathway regulation through gene set analysis. Gene Ontology (GO) enrichment analysis using Ingenuity

Pathway Analysis (IPA; Ingenuity Systems) identified significantly enriched pathways upon miR-132 overexpression in each of the seven cell subpopulations (Figure S7D), suggesting that miR-132 regulation, although subtle at the single-gene level, may concomitantly affect diverse cellular processes. To gain empirical support for this notion, we used the human Ren-Cell line to validate putative miR-132 targets. To prioritize possible direct targets, we selected 150 of the most downregulated transcripts in single NSCs (RGL cells) upon miR-132 overexpression. Using three prediction algorithms for miRNA target identification (Targetscan, DIANA, and PicTar), we extracted a list of 52 predicted miR-132 targets (predicted by at least one of the three algorithms) for semiquantitative real-time PCR validation in RenCells transfected with either a miR-132 mimic or a control oligonucleotide. Interestingly, there was significant downregulation of five mRNAs: *DOCK1* (dedicator of cytokinesis 1), *EPHB3* (ephrin receptor B3), *BTG2* (B cell translocation gene anti-proliferation factor 2), *CAMK1* (calcium/calmodulin-dependent protein kinase 1), and *RAC1* (Ras-related C3 botulinum toxin substrate 1) (Figure 6C), suggesting that these transcripts may be part of the direct effectors of the miR-132-regulated molecular network that generates proneurogenic signals in the RGL NSCs.

Boosting miR-132 levels restores AHN-related memory deficits in old AD mice

To address the functional impact of AHN regulation by miR-132 on relevant memory functions, we assessed the effect of miR-132 overexpression in 9-month-old *App*^{NL-G-F} mice in a passive avoidance test and in a pattern separation, differential fear conditioning-based test (van Boxelaere et al., 2017). Age-matched wild-type mice were used as controls, and animals were i.c.v. injected with either a negative control oligonucleotide or a synthetic miR-132 mimic before behavioral testing (Figure S6E). In passive avoidance, AD mice exhibited decreased latency time to enter the conditioning chamber compared with wild-type animals during the testing phase, suggesting impaired contextual memory (Figure 7A). No change was observed between controls and miR-132-overexpressing wild-type mice (Figure 7A). Interestingly, boosting miR-132 levels in the AD mice rescued this deficit and restored latency time to wild-type levels (Figure 7A). In contrast, after repeated contextual conditioning in a pattern separation test (Figures 7B and 7C), AD mice showed similar contextual fear memory as wild-type animals, and elevating miR-132 levels had no effect on contextual discrimination between two very distinct contexts (Figure 7D, contexts A and C). These results indicate that repeated conditioning establishes context-specific memory traces also in the AD animals, while boosting miR-132 levels has no effect on specific contextual memory. However, discriminating between highly similar contexts (contexts A and B) relies on pattern separation, which is dependent upon the firing properties of the adult-born neurons

(F–H) Quantification of BrdU⁺ (F), Ki-67⁺ (G), and DCX⁺ cells (H) in the dentate gyrus of control (Ctr)- or miR-132-injected, sedentary or running *App*^{NL-G-F} mice at 9 months of age. n = 6–10 mice per group.

(I) Semiquantitative real-time PCR of *Pax6*, *Mki67*, and *Dcx* levels in GFP⁺ cells sorted from the dentate gyrus of Nestin:GFP mice at 3 months of age upon control or miR-132 injection. n = 5 or 6 mice per group.

Values are presented as mean ± SEM. For data analysis, two-way ANOVA with Tukey's post hoc test for multiple comparisons was applied in (B)–(D) and (F)–(H), while Student's t test was used in (I). See also Figures S6 and S7A.

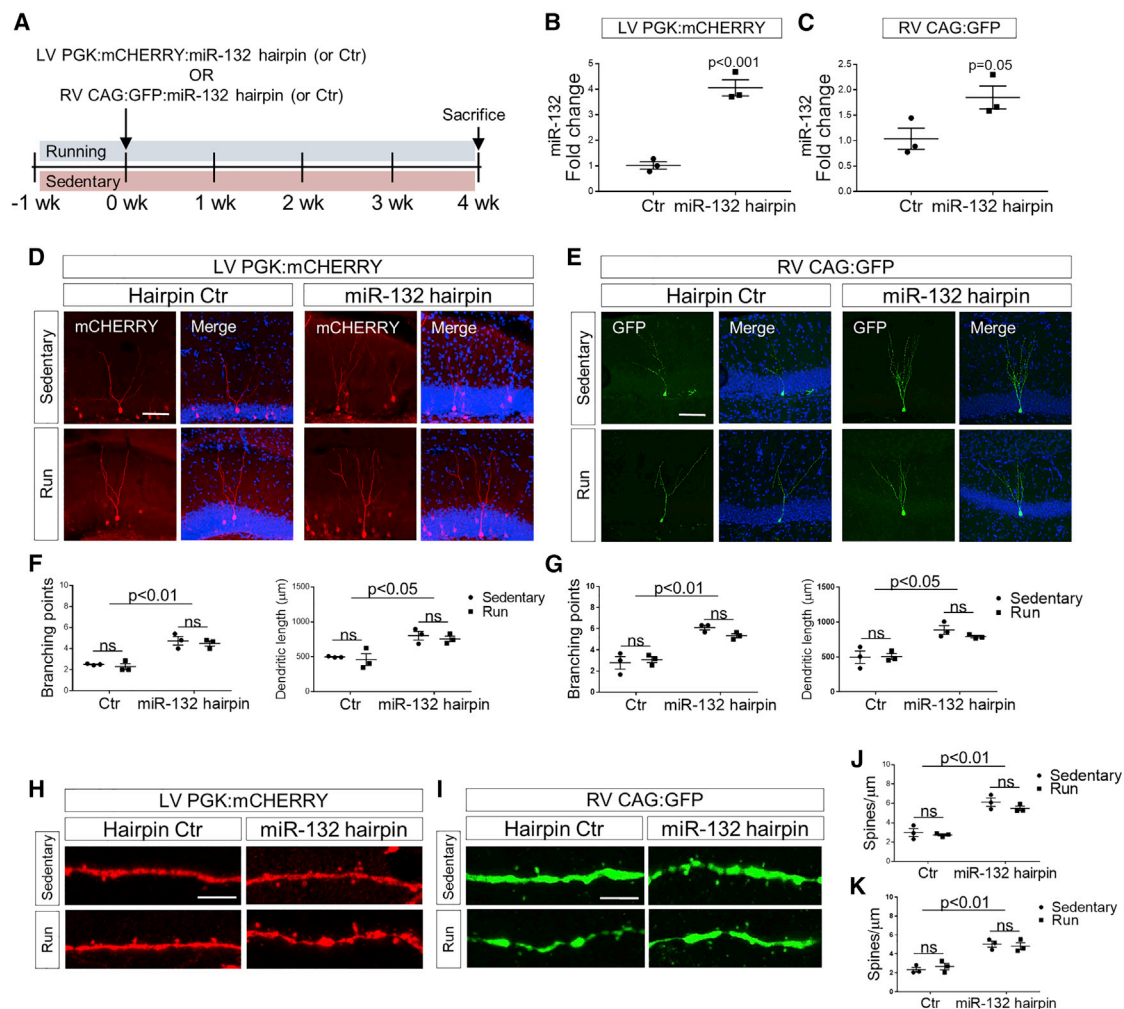


Figure 5. Cell-autonomous effects of miR-132 in adult-born neurons in AD mouse brain

(A) Schematic diagram of the experimental design. Lentiviral and retroviral vectors were used for stereotaxic injections into the dentate gyrus of 9-month-old *App^{NL-G-F}* mice. Animals were housed under sedentary or running conditions and were euthanized 4 weeks post-injection.

(B and C) Semiquantitative real-time PCR of miR-132 in FACS-sorted mCHERRY⁺ cells (B) or dentate gyri (C) upon miR-132 overexpression compared with the respective control vector injections. n = 3 mice per group.

(D and E) Immunolabeling of mCHERRY⁺ (D) or GFP⁺ (E) 4-week-old neurons upon lentiviral (D) or retroviral (E) miR-132 overexpression in *App^{NL-G-F}* animals, under sedentary or running conditions. “Merge” indicates images obtained from overlaying images separately acquired with distinct channels (blue is DAPI).

(F and G) Quantification of dendritic complexity and length in 4-week-old neurons upon miR-132 lentiviral (F) or retroviral (G) overexpression in *App^{NL-G-F}* animals under sedentary or running conditions. n = 3 mice per group; four to six cells per mouse.

(H and I) Imaging of dendritic spines in 4-week-old neurons upon miR-132 lentiviral (H) or retroviral (I) overexpression in *App^{NL-G-F}* animals under sedentary or running conditions.

(J and K) Quantification of spine density in 4-week-old neurons upon miR-132 lentiviral (J) or retroviral (K) overexpression in *App^{NL-G-F}* animals, under sedentary or running conditions. n = 3 mice per group; one dendrite per cell; four to six cells per mouse.

Scale bars, 50 μm (D and E) and 10 μm (H and I). Values are presented as mean ± SEM. For data analysis, two-way ANOVA with Tukey’s post hoc test for multiple comparisons was applied in (F), (G), (J), and (K), while Student’s t test was used in (B) and (C).

in the dentate gyrus. In this test, wild-type controls displayed discriminatory levels of freezing in contexts A and B, while AD animals were unable to distinguish between the two overlapping contexts (Figure 7E). Interestingly, miR-132 overexpression in *App^{NL-G-F}* mice restored performance in the pattern separation test (Figure 7E), suggesting that the positive regulation of AHN by miR-132 can promote cognitive recovery in AD. However, overexpressing miR-132 in wild-type mouse brain resulted in poor performance compared with the control-injected group

(Figure 7E), which could indicate a possible requirement for a dose window for the miR-132 positive effect.

We then addressed the possible contribution of AHN to the beneficial effect of miR-132 in the passive avoidance test in the AD mice. We used the DNA-alkylating agent temozolomide (TMZ), which has been previously shown to repress AHN and context discrimination (Egeland et al., 2017; Garthe et al., 2009; McAvoy et al., 2016; Niibori et al., 2012), to block cell proliferation in control- and miR-132-injected *App^{NL-G-F}* mice (Figure 7F).

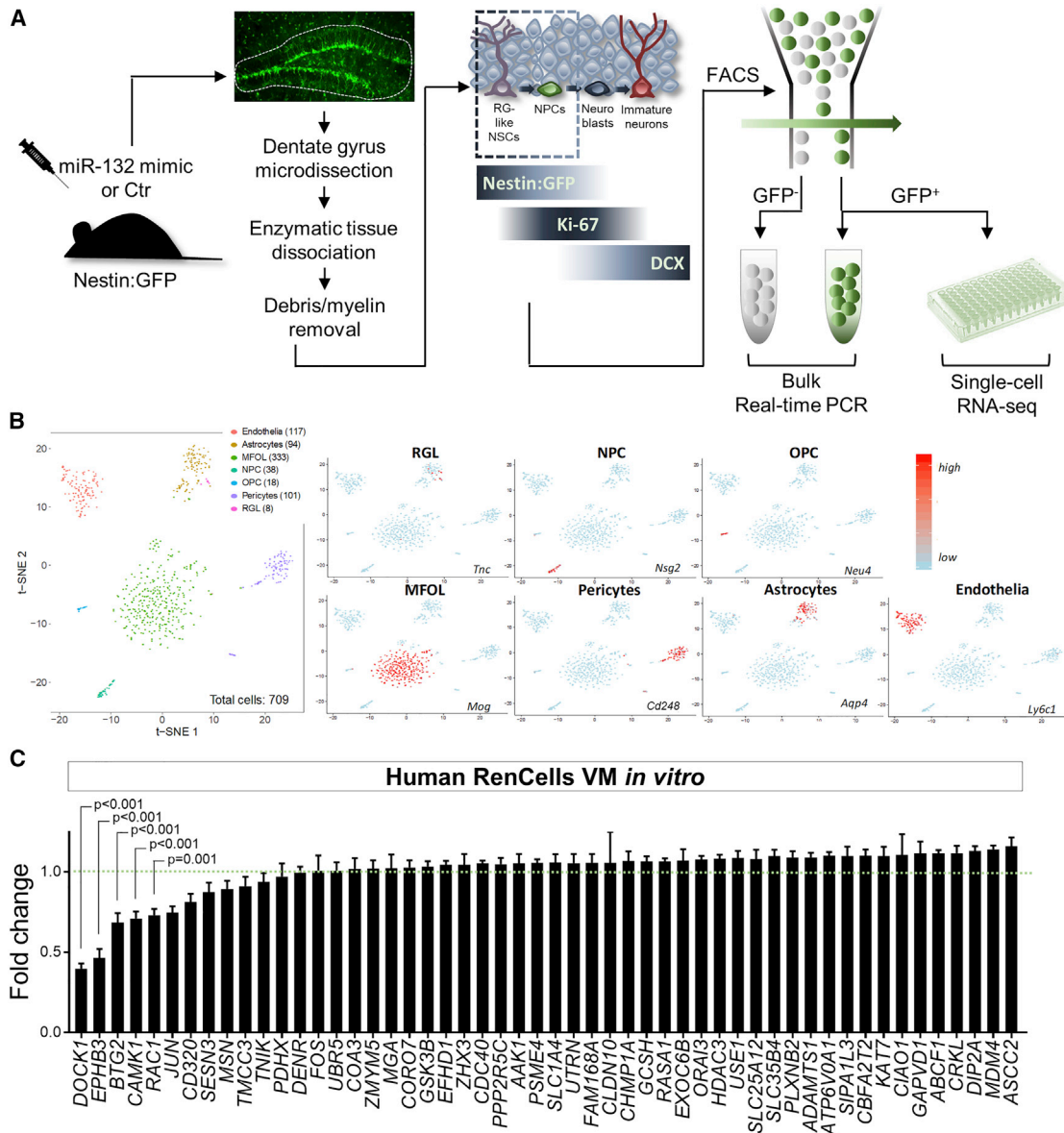


Figure 6. Single-cell approach to identify miR-132 targets in AHN

(A) Schematic diagram of the experimental workflow used to isolate and analyze adult Nestin:GFP⁺ niche cells from the mouse dentate gyrus upon miR-132 overexpression.

(B) Unsupervised hierarchical clustering of dataset, cell type mapping, and cell-type-specific marker expression. Cell numbers per cluster are indicated in parentheses.

(C) Semiquantitative real-time PCR assessment of predicted miR-132 target transcripts in the human RenCell line upon transfection with miR-132 mimic or a control oligonucleotide. $n = 3$ independent experiments. RGL, radial glia-like; NPC, neuronal intermediate progenitor cell; OPC, oligodendrocyte precursor; MFOL, myelin-forming oligodendrocyte. Two-way ANOVA with Tukey's post hoc test for multiple comparisons was used. Dashed line indicates mean fold change of control samples set at 1.

Values are presented as mean \pm SEM. See also [Figure S7](#) and [Tables S5](#) and [S6](#).

Ki-67⁺ and DCX⁺ cell counts at the subgranular zone of the dentate gyrus were used as a readout of the efficiency of proliferation inhibition of adult NPCs ([Figures 7G, 7H, S6F, and S6G](#)). Blocking proliferation in miR-132-overexpressing AD mice abolished memory rescue in the passive avoidance task ([Figure 7I](#)), thereby providing indirect evidence that AHN may be a prime component of miR-132 regulation on contextual memory performance in this

task. These results suggest that replacing miR-132 levels in the AD brain can restore AHN-related memory deficits.

DISCUSSION

Whether AHN is affected in AD brain and, even more fundamentally, whether AHN occurs in adult and aging human brain at all,

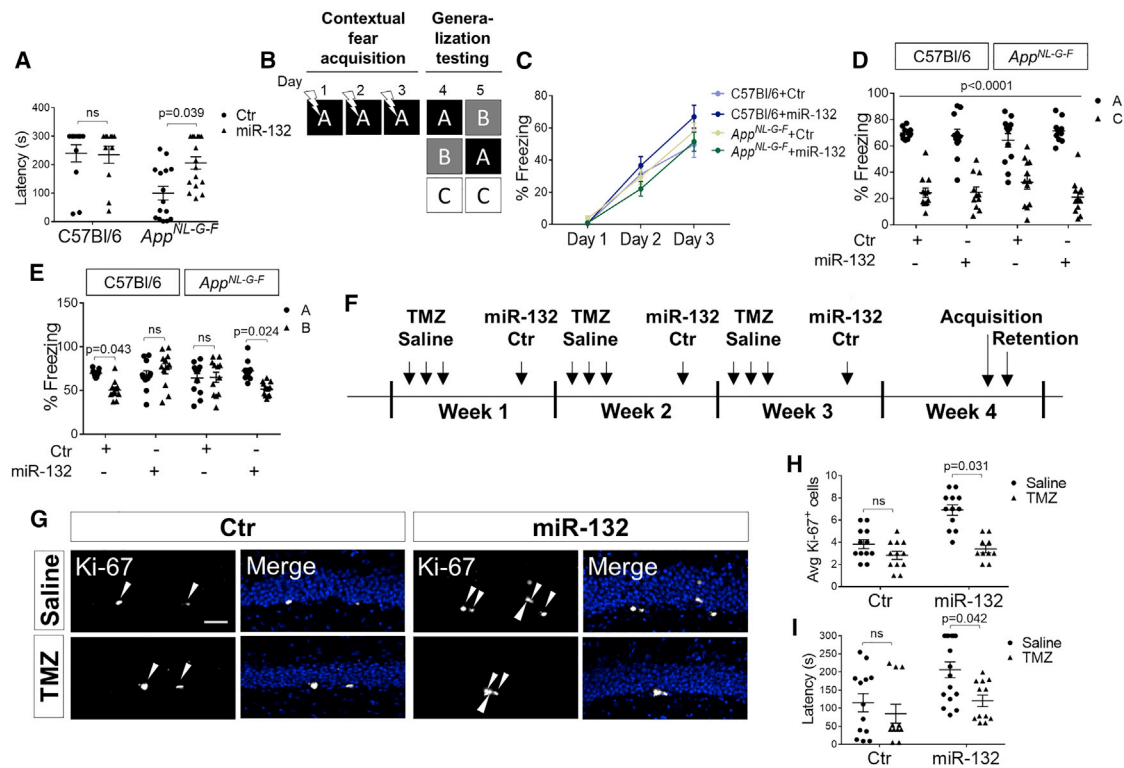


Figure 7. miR-132 overexpression restores memory deficits in AD mice

(A) Latency time (indicated in seconds) in passive avoidance test upon control or miR-132 injections in wild-type and AD mice. (B) Schematic diagram of pattern separation test. Mice were fear-conditioned for 3 days in shock-receiving context A and subsequently tested for their ability to discriminate between similar contexts A and B and between different contexts A and C. (C) Percentage of time spent freezing by control (Ctr)- or miR-132-injected 9-month-old wild-type (C57BL/6) or *App^{NL-G-F}* mice during days 1–3 of fear acquisition. (D and E) Percentage of time spent freezing in contexts A and C (D) or A and B (E) during days 4 and 5 of generalization testing. $n = 12$ –15 mice per group. (F) Schematic diagram of passive avoidance test in 9-month-old *App^{NL-G-F}* mice using saline or temozolomide (TMZ) intraperitoneal (i.p.) injections and control (Ctr) or miR-132 (miR-132) intracerebroventricular injections. (G) Ki-67 immunolabeling in the dentate gyrus of saline or TMZ-, Ctr-, or miR-132-injected *App^{NL-G-F}* mice after passive avoidance test completion. “Merge” indicates images obtained from overlaying images separately acquired with distinct channels (blue is DAPI). Arrowheads indicate Ki-67⁺-cells. (H) Quantification of Ki-67⁺ cells upon saline or TMZ injections in Ctr- or miR-132-injected *App^{NL-G-F}* mice. $n = 11$ –13 mice per group. Scale bar, 50 μm . (I) Latency time in passive avoidance test in saline or TMZ-, Ctr-, or miR-132-injected *App^{NL-G-F}* mice. Values are presented as mean \pm SEM. $n = 11$ –13 mice per group. For data analysis, two-way ANOVA with Tukey’s post hoc test for multiple comparisons was used. See also Figure S6.

has been a returning issue of controversy (Boldrini et al., 2018; Eriksson et al., 1998; Gatt et al., 2019; Kempermann et al., 2018; Knoth et al., 2010; Lucassen et al., 2020a, 2020b; Paredes et al., 2018; Snyder, 2019; Sorrells et al., 2018; Spalding et al., 2013; Tartt et al., 2018). The discussion has illustrated the paramount importance of accurate interpretation of histological findings, sample stratification, postmortem delay, tissue preservation, marker labeling methodology, and inclusion of stereology during data analysis (Kempermann et al., 2018; Lucassen et al., 2020a, 2020b). Notably, two recent reports using high-quality human postmortem brain samples and refined methodological approaches have now firmly established that adult neurogenesis occurs in human brain. These studies demonstrated that AHN can still be detected in centenarians and that AHN drops dramatically in AD patients (Moreno-Jiménez et al., 2019; Tobin et al., 2019), setting the stage for the functional studies in two mouse models of AD reported here.

We show that the running-induced miR-132 upregulation in the hippocampal neurogenic niche becomes compromised with pa-

thology progression, independently of gender, and that these alterations are paralleled by decreased neurogenic potential. The hippocampal neurogenic niche involves a complex network of intercellular communication and molecular regulatory signals, which is receptive to extrinsic and intrinsic cues, such as experience, exercise, aging, and increased neuroinflammation (Fuster-Matanzo et al., 2013; Mosher and Schaffer, 2018; Villeda et al., 2011). Our data demonstrate that treatment of human neuronal precursor cells with oligomeric A β reduces proliferation and miR-132 expression, consistent with several lines of evidence suggesting that A β per se affects the neurogenic potential of NSCs and progenitors (Haughey et al., 2002; He et al., 2013; Lee et al., 2013). Serum obtained from sporadic AD cases also elicited a significant reduction of miR-132 in hippocampal human NSCs. This can be attributed to A β oligomers or other AD-related systemic signals.

In an attempt to identify relevant transcriptomic targets of miR-132 at the adult hippocampal neurogenic niche, we performed single-cell transcriptome analysis of the Nestin:GFP-positive

niche-residing cells isolated from the dentate gyrus of mice overexpressing miR-132 and further validated possible regulatory interactions in human NSCs *in vitro*. This approach revealed a miR-132-specific molecular signature consisting of *DOCK1*, *EPHB3*, *BTG2*, *CAMK1*, and *RAC1*, all of which have reported roles in neuronal differentiation and function (Fortin et al., 2010; Goid and Nicoll, 2010; Pillat et al., 2016; Theus et al., 2010; Vadodaria et al., 2013; Yang et al., 2012). Dock1, Ephb3, Camk1, and Rac1 have additionally been implicated in AD (Aguilar et al., 2017; Becker et al., 2014; Overk and Masliah, 2014; Riascos et al., 2014), while all five proteins have been associated with the immune response in a variety of cells (D'Ambrosi et al., 2014; Goid and Nicoll, 2010; Guo et al., 2013; Naskar et al., 2014; Pillat et al., 2016; Theus et al., 2010; Yuniati et al., 2019). Interestingly, miR-132 knockdown also repressed the running-induced increase of *Bdnf*, a key neurotrophic factor contributing to the fitness of the niche and the neurogenic potential. Of note, miR-132 overexpression in human neuronal precursors *in vitro* and adult mouse NSCs and progenitors *in vivo* induced neuronal differentiation and maturation in a cell-autonomous manner. Collectively, these observations suggest that the proneurogenic effects of miR-132 may be effectuated at the level of NPC proliferation, neuronal differentiation, survival, functional integration, neurotrophic boost, or a combination thereof, possibly depending on the presence or absence of distinct stimuli.

Adult-born neurons facilitate the spatiotemporal contextualization of information and they help avoid catastrophic interference in the hippocampal network, by promoting “behavioral pattern separation” (Kempermann et al., 2018). Poor performance in pattern separation tasks in AD patients (Ally et al., 2013; Wesnes et al., 2014; Yassa et al., 2010) and preserved AHN in non-demented individuals with AD or MCI neuropathology have been reported (Briley et al., 2016; Tobin et al., 2019). We confirm here that features of hippocampus-dependent functions that are related to context fear conditioning and avoidance tasks, which are linked to deficient AHN in the context of an AD mouse model, can be rescued by restoring miR-132 levels in the brain of these mice.

Intriguingly, miR-132 overexpression in wild-type mice resulted in a worsening of performance in the AHN-specific pattern separation task, suggesting that miR-132 expression should be maintained within a certain range to ensure proper learning and memory function. This observation confirms previous results, in which “supra-physiological” (>3-fold) miR-132 levels inhibit hippocampus-dependent memory in wild-type mice (Hansen et al., 2013). Thus, further work is required to assess a therapeutically relevant window for miR-132 overexpression in AD brain.

In conclusion, our data support a model in which miR-132 acts as a proneurogenic signal transducer contributing to specific aspects of memory formation. AD pathology leads to miR-132 deficiency and ultimately compromises AHN. Recently, induction of AHN in conjunction with improvement of the microenvironment of the adult hippocampal niche via BDNF overexpression was put forward as a putative target for therapeutic intervention in AD (Choi et al., 2018). Moreover, recent groundbreaking advances in the treatment of neurodegenerative disorders using small RNA-based therapeutics in spinal muscular atrophy (Finkel et al., 2016) may also pave the way for more direct miR-132-based therapeutic approaches in AD. Dose finding will be crucial, while delineating the molecular

and cellular mechanisms underlying the neurogenic effects of miR-132 may provide impetus for identifying novel strategies to therapeutically harness AHN in AD.

Limitations of the study

We used two AD amyloidosis mouse models carrying familial AD mutations and cultures of human NSCs incubated with synthetic A β , and hence, our study primarily addresses the effects of AD pathology pertinent to amyloidosis. The impact of other pathological endophenotypes of (sporadic) AD on miR-132 and AHN was not explored. Our histological analysis in human brain material was not systematic; for a more thorough characterization of AHN in human AD brain, readers should refer to Moreno-Jiménez et al. (2019) and Tobin et al. (2019). Last, further and more powered single-cell transcriptomic studies will be required to systematically explore the cell-type-specific effects of miR-132 at the adult hippocampal neurogenic niche.

STAR★METHODS

Detailed methods are provided in the online version of this paper and include the following:

- KEY RESOURCES TABLE
- RESOURCE AVAILABILITY
 - Lead contact
 - Materials availability
 - Data and code availability
- EXPERIMENTAL MODEL AND SUBJECT DETAILS
 - Animals
 - Human samples
 - Human cell lines
- METHOD DETAILS
 - Intracerebroventricular (i.c.v.) injections
 - Viral vector injections into the dentate gyrus
 - Induction of AHN via voluntary running
 - 5-bromo-2'-deoxyuridine (BrdU) injections
 - Immunofluorescence in mouse brain sections and cultured cells
 - Immunostaining of human hippocampal sections
 - Tissue clearing
 - Fluorescence *in situ* hybridization (FISH)
 - Image acquisition, processing and analysis
 - RenCell transfections
 - Neural induction of human embryonic pluripotent stem cells
 - Preparation of A β_{1-42} oligomers and neuronal precursor cell treatment
 - Treatment of human neuronal precursor cells with AD and control serum
 - RNA isolation, reverse transcription and real-time PCR
 - Adult dentate gyrus dissociation for fluorescence activated cell sorting (FACS) of Nestin:GFP⁺ cells
 - Behavioral testing
 - Temozolomide (TMZ) treatment
 - Smart-seq2 processing and single-cell library preparation
 - Data processing
- QUANTIFICATION AND STATISTICAL ANALYSIS

SUPPLEMENTAL INFORMATION

Supplemental information can be found online at <https://doi.org/10.1016/j.stem.2021.05.001>.

ACKNOWLEDGMENTS

We thank Véronique Hendrickx and Jonas Verwaeren for animal husbandry; Sebastian Munck, Nikky Corthout, Axelle Kerstens (LiMoNe, VIB), the VIB Nucleomics Core of Leuven, the VIB-KU Leuven FACS Core, An Snellinx, Isabel Salas, Dries T'Syen, Sara Calafate, Jeroen Vanderlinden, Natalia Gunko, Dorien Vandael, Annette Gärtner, and Jenny Peeters for providing technical assistance and resources; and Annerieke Sierksma, Patrik Verstreken, Laure Bally-Cuif, Joris De Wit, Pierre Vanderhaeghen, and Matthew Holt for critical discussions and feedback. The *APP/PS1* mice were a kind gift from Mathias Jucker (DZNE, Germany), the *App^{NL-G-F}* mice were kindly provided by Takaomi Saido (RIKEN Brain Science Institute, Japan), and the Nestin:GFP mice were from Grigori Enikolopov (Stony Brook University, New York). The PGK lentiviral vector was a kind gift from Antonella Consiglio. Part of the graphical abstract was created with BioRender.com. H.W. is a Fonds voor Wetenschappelijk Onderzoek – Vlaanderen (FWO) Scholar and receives funding from B-SMART European Union (EU) Horizon 2020 and Stichting Alzheimer Onderzoek, Belgium (SAO). D.R.T. is funded by grants from FWO (G0F8516N Odysseus) and VIND (IWT 135043). Work in the S.T. lab is supported by U.K. Medical Research Council grants MR/N030087/1 and MR/S00484X/1. H.Z. is a Wallenberg Scholar. Work in the B.D.S. laboratory is supported by a European Research Council (ERC) grant ERC-2010-AG_268675, FWO, KU Leuven, VIB, Stichting Alzheimer Onderzoek, Belgium (SAO), the Elisabeth Foundation, VIND (IWT 135043), and a Methusalem grant from KU Leuven and the Flemish Government. B.D.S. is the Bax-Vanluffelen Chair for Alzheimer's Disease and is supported directly by the Opening the Future campaign of Leuven Universiteit Fonds. E. Salta has previously received funding from FWO, the Alzheimer's Association (AA), and Stichting Alzheimer Onderzoek, Belgium (SAO). Work in the E. Salta lab is currently supported by Alzheimer Nederland, Health-Holland, and the AA.

AUTHOR CONTRIBUTIONS

Conceptualization, H.W., B.D.S., and E. Salta; Methodology, H.W., S.B., K.C., L.W., Z.C.-V., R.D.H., D.R.T., E. Silajdžić, S.T., C.S.F., B.D.S., and E. Salta; Investigation, H.W., S.B., S.S., E.V.E., K.C., K.H., L.W., A.R., E. Silajdžić, A.P., G.T., C.S.F., and E. Salta; Software, M.F., N.T., and Y.F.; Formal Analysis, M.F., N.T., Y.F., and E. Salta; Resources, Z.C.-V., R.D.H., D.R.T., H.Z., and S.T.; Writing – Review & Editing, E. Salta and B.D.S., with input from all authors; Supervision, E. Salta and B.D.S.; Funding Acquisition, E. Salta and B.D.S.

DECLARATION OF INTERESTS

The authors declare no competing interests.

Received: March 17, 2021

Revised: April 24, 2021

Accepted: April 30, 2021

Published: May 24, 2021

SUPPORTING CITATIONS

The following references appear in the supplemental information: Braak et al., (2006), Hyman et al., (2012), Johansson et al., (2013), Mirra et al., (1991), Morris, (1993), Rijal Upadhaya et al., (2014), Thal et al., (2000).

REFERENCES

Aguilar, B.J., Zhu, Y., and Lu, Q. (2017). Rho GTPases as therapeutic targets in Alzheimer's disease. *Alzheimers Res. Ther.* 9, 97.
Ally, B.A., Hussey, E.P., Ko, P.C., and Molitor, R.J. (2013). Pattern separation and pattern completion in Alzheimer's disease: evidence of rapid forgetting in amnesic mild cognitive impairment. *Hippocampus* 23, 1246–1258.

Anacker, C., and Hen, R. (2017). Adult hippocampal neurogenesis and cognitive flexibility—linking memory and mood. *Nat. Rev. Neurosci.* 18, 335–346.

Artegiani, B., Lyubimova, A., Muraro, M., van Es, J.H., van Oudenaarden, A., and Clevers, H. (2017). A single-cell RNA sequencing study reveals cellular and molecular dynamics of the hippocampal neurogenic niche. *Cell Rep.* 21, 3271–3284.

Baptista, P., and Andrade, J.P. (2018). Adult hippocampal neurogenesis: regulation and possible functional and clinical correlates. *Front. Neuroanat.* 12, 44.

Becker, T., Ramirez, A., Herold, C., van Duijn, C., Schellenberg, G.D., Williams, J., Amouyel, P., Yang, Q., Seshadri, S., and van der Lee, S.J. (2014). Comprehensive gene-gene interaction meta-analysis of IGAP GWA studies. *Alzheimers Dement.* 10, 245.

Boldrini, M., Fulmore, C.A., Tartt, A.N., Simeon, L.R., Pavlova, I., Poposka, V., Rosoklija, G.B., Stankov, A., Arango, V., Dwork, A.J., et al. (2018). Human hippocampal neurogenesis persists throughout aging. *Cell Stem Cell* 22, 589–599.e5.

Bond, A.M., Ming, G.L., and Song, H. (2015). Adult mammalian neural stem cells and neurogenesis: five decades later. *Cell Stem Cell* 17, 385–395.

Braak, H., Alafuzoff, I., Arzberger, T., Kretschmar, H., and Del Tredici, K. (2006). Staging of Alzheimer disease-associated neurofibrillary pathology using paraffin sections and immunocytochemistry. *Acta Neuropathol.* 112, 389–404.

Briley, D., Ghirardi, V., Woltjer, R., Renck, A., Zolochovska, O., Tagliatalata, G., and Micci, M.-A. (2016). Preserved neurogenesis in non-demented individuals with AD neuropathology. *Sci. Rep.* 6, 27812.

Brkic, M., Balusu, S., Van Wonterghem, E., Gorié, N., Benilova, I., Kremer, A., Van Hove, I., Moons, L., De Strooper, B., Kanazir, S., et al. (2015). Amyloid β oligomers disrupt blood-CSF barrier integrity by activating matrix metalloproteinases. *J. Neurosci.* 35, 12766–12778.

Butler, A., Hoffman, P., Smibert, P., Papalexí, E., and Satija, R. (2018). Integrating single-cell transcriptomic data across different conditions, technologies, and species. *Nat. Biotechnol.* 36, 411–420.

Callaerts-Vegh, Z., Ahmed, T., Vermaercke, B., Marynen, P., Balschun, D., Froyen, G., and D'Hooge, R. (2015). Nxf7 deficiency impairs social exploration and spatio-cognitive abilities as well as hippocampal synaptic plasticity in mice. *Front. Behav. Neurosci.* 9, 179.

Choi, S.H., Bylykbashí, E., Chatila, Z.K., Lee, S.W., Pulli, B., Clemenson, G.D., Kim, E., Rompala, A., Oram, M.K., Asselin, C., et al. (2018). Combined adult neurogenesis and BDNF mimic exercise effects on cognition in an Alzheimer's mouse model. *Science* 361, eaan8821.

Cipriani, S., Ferrer, I., Aronica, E., Kovacs, G.G., Verney, C., Nardelli, J., Khung, S., Delezoide, A.-L., Milenkovic, I., Rasika, S., et al. (2018). Hippocampal radial glial subtypes and their neurogenic potential in human fetuses and healthy and Alzheimer's disease adults. *Cereb. Cortex* 28, 2458–2478.

Clelland, C.D., Choi, M., Romberg, C., Clemenson, G.D., Fragniere, A., Tyers, P., Jessberger, S., Saksida, L.M., Barker, R.A., Gage, F.H., et al. (2009). A functional role for adult hippocampal neurogenesis in spatial pattern separation. *Science* 325, 210–213.

Coras, R., Siebzehnrubl, F.A., Pauli, E., Huttner, H.B., Njunting, M., Kobow, K., Villmann, C., Hahnen, E., Neuhuber, W., Weigel, D., et al. (2010). Low proliferation and differentiation capacities of adult hippocampal stem cells correlate with memory dysfunction in humans. *Brain* 133, 3359–3372.

D'Ambrosi, N., Rossi, S., Gerbino, V., and Cozzolino, M. (2014). Rac1 at the crossroad of actin dynamics and neuroinflammation in Amyotrophic Lateral Sclerosis. *Front. Cell. Neurosci.* 8, 279.

D'Hooge, R., Lüllmann-Rauch, R., Beckers, T., Balschun, D., Schwake, M., Reiss, K., von Figura, K., and Saftig, P. (2005). Neurocognitive and psychotiform behavioral alterations and enhanced hippocampal long-term potentiation in transgenic mice displaying neuropathological features of human alpha-mannosidosis. *J. Neurosci.* 25, 6539–6549.

Danielson, N.B., Kaifosh, P., Zaremba, J.D., Lovett-Barron, M., Tsai, J., Denny, C.A., Balough, E.M., Goldberg, A.R., Drew, L.J., Hen, R., et al. (2016). Distinct contribution of adult-born hippocampal granule cells to context encoding. *Neuron* 90, 101–112.

- Dickey, C.A., Loring, J.F., Montgomery, J., Gordon, M.N., Eastman, P.S., and Morgan, D. (2003). Selectively reduced expression of synaptic plasticity-related genes in amyloid precursor protein + presenilin-1 transgenic mice. *J. Neurosci.* 23, 5219–5226.
- Dobin, A., Davis, C.A., Schlesinger, F., Drenkow, J., Zaleski, C., Jha, S., Batut, P., Chaisson, M., and Gingeras, T.R. (2013). STAR: ultrafast universal RNA-seq aligner. *Bioinformatics* 29, 15–21.
- Edbauer, D., Neilson, J.R., Foster, K.A., Wang, C.F., Seeburg, D.P., Battersby, M.N., Tada, T., Dolan, B.M., Sharp, P.A., and Sheng, M. (2010). Regulation of synaptic structure and function by FMRP-associated microRNAs miR-125b and miR-132. *Neuron* 65, 373–384.
- Egeland, M., Guinaudie, C., Du Preez, A., Musaelyan, K., Zunszain, P.A., Fernandes, C., Pariante, C.M., and Thuret, S. (2017). Depletion of adult neurogenesis using the chemotherapy drug temozolomide in mice induces behavioural and biological changes relevant to depression. *Transl. Psychiatry* 7, e1101.
- El Fatimy, R., Li, S., Chen, Z., Mushannen, T., Gongala, S., Wei, Z., Balu, D.T., Rabinovsky, R., Cantlon, A., Elkhal, A., et al. (2018). MicroRNA-132 provides neuroprotection for tauopathies via multiple signaling pathways. *Acta Neuropathol.* 136, 537–555.
- Eriksson, P.S., Perfilieva, E., Björk-Eriksson, T., Alborn, A.M., Nordborg, C., Peterson, D.A., and Gage, F.H. (1998). Neurogenesis in the adult human hippocampus. *Nat. Med.* 4, 1313–1317.
- Espuny-Camacho, I., Michelsen, K.A., Gall, D., Linaro, D., Hasche, A., Bonnefont, J., Bali, C., Orduz, D., Bilheu, A., Herpoel, A., et al. (2013). Pyramidal neurons derived from human pluripotent stem cells integrate efficiently into mouse brain circuits in vivo. *Neuron* 77, 440–456.
- Espuny-Camacho, I., Arranz, A.M., Fiers, M., Snellinx, A., Ando, K., Munck, S., Bonnefont, J., Lambot, L., Corthout, N., Omodho, L., et al. (2017). Hallmarks of Alzheimer's disease in stem-cell-derived human neurons transplanted into mouse brain. *Neuron* 93, 1066–1081.e8.
- Finkel, R.S., Chiriboga, C.A., Vajsar, J., Day, J.W., Montes, J., De Vivo, D.C., Yamashita, M., Rigo, F., Hung, G., Schneider, E., et al. (2016). Treatment of infantile-onset spinal muscular atrophy with nusinersen: a phase 2, open-label, dose-escalation study. *Lancet* 388, 3017–3026.
- Fortin, D.A., Davare, M.A., Srivastava, T., Brady, J.D., Nygaard, S., Derkach, V.A., and Soderling, T.R. (2010). Long-term potentiation-dependent spine enlargement requires synaptic Ca²⁺-permeable AMPA receptors recruited by CaM-kinase I. *J. Neurosci.* 30, 11565–11575.
- Fuster-Matanzo, A., Llorens-Martín, M., Hernández, F., and Avila, J. (2013). Role of neuroinflammation in adult neurogenesis and Alzheimer disease: therapeutic approaches. *Mediators Inflamm.* 2013, 260925.
- Garthe, A., Behr, J., and Kempermann, G. (2009). Adult-generated hippocampal neurons allow the flexible use of spatially precise learning strategies. *PLoS ONE* 4, e5464.
- Gatt, A., Lee, H., Williams, G., Thuret, S., and Ballard, C. (2019). Expression of neurogenic markers in Alzheimer's disease: a systematic review and metatranscriptomic analysis. *Neurobiol. Aging* 76, 166–180.
- Goold, C.P., and Nicoll, R.A. (2010). Single-cell optogenetic excitation drives homeostatic synaptic depression. *Neuron* 68, 512–528.
- Guo, L., Stripay, J.L., Zhang, X., Collage, R.D., Hulver, M., Carchman, E.H., Howell, G.M., Zuckerbraun, B.S., Lee, J.S., and Rosengart, M.R. (2013). CaMKI α regulates AMP kinase-dependent, TORC1-independent autophagy during lipopolysaccharide-induced acute lung neutrophilic inflammation. *J. Immunol.* 190, 3620–3628.
- Hagihara, H., Toyama, K., Yamasaki, N., and Miyakawa, T. (2009). Dissection of hippocampal dentate gyrus from adult mouse. *J. Vis. Exp.* 33, 1543.
- Hansen, K.F., Karelina, K., Sakamoto, K., Wayman, G.A., Impey, S., and Obrietan, K. (2013). miRNA-132: a dynamic regulator of cognitive capacity. *Brain Struct. Funct.* 218, 817–831.
- Hansen, K.F., Sakamoto, K., Aten, S., Snider, K.H., Loeser, J., Hesse, A.M., Page, C.E., Pelz, C., Arthur, J.S.C., Impey, S., and Obrietan, K. (2016). Targeted deletion of miR-132/-212 impairs memory and alters the hippocampal transcriptome. *Learn. Mem.* 23, 61–71.
- Haughey, N.J., Nath, A., Chan, S.L., Borchard, A.C., Rao, M.S., and Mattson, M.P. (2002). Disruption of neurogenesis by amyloid beta-peptide, and perturbed neural progenitor cell homeostasis, in models of Alzheimer's disease. *J. Neurochem.* 83, 1509–1524.
- He, N., Jin, W.-L., Lok, K.-H., Wang, Y., Yin, M., and Wang, Z.-J. (2013). Amyloid- β (1-42) oligomer accelerates senescence in adult hippocampal neural stem/progenitor cells via formylpeptide receptor 2. *Cell Death Dis.* 4, e924.
- Hébert, S.S., Wang, W.X., Zhu, Q., and Nelson, P.T. (2013). A study of small RNAs from cerebral neocortex of pathology-verified Alzheimer's disease, dementia with lewy bodies, hippocampal sclerosis, frontotemporal lobar dementia, and non-demented human controls. *J. Alzheimers Dis.* 35, 335–348.
- Hernandez-Rapp, J., Smith, P.Y., Filali, M., Goupil, C., Planel, E., Magill, S.T., Goodman, R.H., and Hébert, S.S. (2015). Memory formation and retention are affected in adult miR-132/212 knockout mice. *Behav. Brain Res.* 287, 15–26.
- Hochgerner, H., Zeisel, A., Lönnerberg, P., and Linnarsson, S. (2018). Conserved properties of dentate gyrus neurogenesis across postnatal development revealed by single-cell RNA sequencing. *Nat. Neurosci.* 21, 290–299.
- Hyman, B.T., Phelps, C.H., Beach, T.G., Bigio, E.H., Cairns, N.J., Carrillo, M.C., Dickson, D.W., Duyckaerts, C., Frosch, M.P., Masliah, E., et al. (2012). National Institute on Aging-Alzheimer's Association guidelines for the neuropathologic assessment of Alzheimer's disease. *Alzheimers Dement.* 8, 1–13.
- Jimenez-Mateos, E.M., Bray, I., Sanz-Rodriguez, A., Engel, T., McKiernan, R.C., Mouri, G., Tanaka, K., Sano, T., Saugstad, J.A., Simon, R.P., et al. (2011). miRNA Expression profile after status epilepticus and hippocampal neuroprotection by targeting miR-132. *Am. J. Pathol.* 179, 2519–2532.
- Johansson, P., Åberg, D., Johansson, J.-O., Mattsson, N., Hansson, O., Åhrén, B., Isgaard, J., Åberg, N.D., Blennow, K., Zetterberg, H., et al. (2013). Serum but not cerebrospinal fluid levels of insulin-like growth factor-I (IGF-I) and IGF-binding protein-3 (IGFBP-3) are increased in Alzheimer's disease. *Psychoneuroendocrinology* 38, 1729–1737.
- Kempermann, G., Gage, F.H., Aigner, L., Song, H., Curtis, M.A., Thuret, S., Kuhn, H.G., Jessberger, S., Frankland, P.W., Cameron, H.A., et al. (2018). Human adult neurogenesis: evidence and remaining questions. *Cell Stem Cell* 23, 25–30.
- Knoth, R., Singec, I., Ditter, M., Pantazis, G., Capetian, P., Meyer, R.P., Horvat, V., Volk, B., and Kempermann, G. (2010). Murine features of neurogenesis in the human hippocampus across the lifespan from 0 to 100 years. *PLoS ONE* 5, e8809.
- Kuperstein, I., Broersen, K., Benilova, I., Rozenski, J., Jonckheere, W., Debulpaep, M., Vandersteen, A., Segers-Nolten, I., Van Der Werf, K., Subramaniam, V., et al. (2010). Neurotoxicity of Alzheimer's disease A β peptides is induced by small changes in the A β 42 to A β 40 ratio. *EMBO J.* 29, 3408–3420.
- Lau, P., Bossers, K., Janky, R., Salta, E., Frigerio, C.S., Barbash, S., Rothman, R., Sierksma, A.S.R., Thathiah, A., Greenberg, D., et al. (2013). Alteration of the microRNA network during the progression of Alzheimer's disease. *EMBO Mol. Med.* 5, 1613–1634.
- Lee, I.-S., Jung, K., Kim, I.-S., and Park, K.I. (2013). Amyloid- β oligomers regulate the properties of human neural stem cells through GSK-3 β signaling. *Exp. Mol. Med.* 45, e60.
- Liao, Y., Smyth, G.K., and Shi, W. (2014). featureCounts: an efficient general purpose program for assigning sequence reads to genomic features. *Bioinformatics* 30, 923–930.
- Liufu, Z., Zhao, Y., Guo, L., Miao, G., Xiao, J., Lyu, Y., Chen, Y., Shi, S., Tang, T., and Wu, C.-I. (2017). Redundant and incoherent regulations of multiple phenotypes suggest microRNAs' role in stability control. *Genome Res.* 27, 1665–1673.
- Livak, K.J., and Schmittgen, T.D. (2001). Analysis of relative gene expression data using real-time quantitative PCR and the 2(-Delta Delta C(T)) Method. *Methods* 25, 402–408.
- Lucassen, P.J., Fitzsimons, C.P., Salta, E., and Maletic-Savatic, M. (2020a). Adult neurogenesis, human after all (again): Classic, optimized, and future approaches. *Behav. Brain Res.* 381, 112458.

- Lucassen, P.J., Toni, N., Kempermann, G., Frisen, J., Gage, F.H., and Swaab, D.F. (2020b). Limits to human neurogenesis—really? *Mol. Psychiatry* **25**, 2207–2209.
- Luikart, B.W., Bensen, A.L., Washburn, E.K., Perederiy, J.V., Su, K.G., Li, Y., Kernie, S.G., Parada, L.F., and Westbrook, G.L. (2011). miR-132 mediates the integration of newborn neurons into the adult dentate gyrus. *PLoS ONE* **6**, e19077.
- Magill, S.T., Cambronne, X.A., Luikart, B.W., Lioy, D.T., Leighton, B.H., Westbrook, G.L., Mandel, G., and Goodman, R.H. (2010). microRNA-132 regulates dendritic growth and arborization of newborn neurons in the adult hippocampus. *Proc. Natl. Acad. Sci. U S A* **107**, 20382–20387.
- Maruszak, A., Murphy, T., Liu, B., de Lucia, C., Douiri, A., Nevado, A.J., Teunissen, C.E., Visser, P.J., Price, J., Lovestone, S., and Thuret, S. (2017). Cellular phenotyping of hippocampal progenitors exposed to patient serum predicts conversion to Alzheimer's disease. *bioRxiv*. <https://doi.org/10.1101/175604>.
- McAvoy, K.M., Scobie, K.N., Berger, S., Russo, C., Guo, N., Decharatanachart, P., Vega-Ramirez, H., Miake-Lye, S., Whalen, M., Nelson, M., et al. (2016). Modulating neuronal competition dynamics in the dentate gyrus to rejuvenate aging memory circuits. *Neuron* **91**, 1356–1373.
- Mignone, J.L., Kukekov, V., Chiang, A.-S., Steindler, D., and Enikolopov, G. (2004). Neural stem and progenitor cells in nestin-GFP transgenic mice. *J. Comp. Neurol.* **469**, 311–324.
- Mirra, S.S., Heyman, A., McKeel, D., Sumi, S.M., Crain, B.J., Brownlee, L.M., Vogel, F.S., Hughes, J.P., van Belle, G., and Berg, L. (1991). The Consortium to Establish a Registry for Alzheimer's Disease (CERAD). Part II. Standardization of the neuropathologic assessment of Alzheimer's disease. *Neurology* **41**, 479–486.
- Moore, M.J., Scheel, T.K.H., Luna, J.M., Park, C.Y., Fak, J.J., Nishiuchi, E., Rice, C.M., and Darnell, R.B. (2015). miRNA-target chimeras reveal miRNA 3'-end pairing as a major determinant of Argonaute target specificity. *Nat. Commun.* **6**, 8864.
- Moreno-Jiménez, E.P., Flor-García, M., Terreros-Roncal, J., Rábano, A., Cafini, F., Pallas-Bazarra, N., Ávila, J., and Llorens-Martín, M. (2019). Adult hippocampal neurogenesis is abundant in neurologically healthy subjects and drops sharply in patients with Alzheimer's disease. *Nat. Med.* **25**, 554–560.
- Morris, J.C. (1993). The Clinical Dementia Rating (CDR): current version and scoring rules. *Neurology* **43**, 2412–2414.
- Mosher, K.I., and Schaffer, D.V. (2018). Influence of hippocampal niche signals on neural stem cell functions during aging. *Cell Tissue Res.* **371**, 115–124.
- Mu, Y., and Gage, F.H. (2011). Adult hippocampal neurogenesis and its role in Alzheimer's disease. *Mol. Neurodegener.* **6**, 85.
- Nakashiba, T., Cushman, J.D., Pelkey, K.A., Renaudineau, S., Buhl, D.L., McHugh, T.J., Rodriguez Barrera, V., Chittajallu, R., Iwamoto, K.S., McBain, C.J., et al. (2012). Young dentate granule cells mediate pattern separation, whereas old granule cells facilitate pattern completion. *Cell* **149**, 188–201.
- Naskar, D., Maiti, G., Chakraborty, A., Roy, A., Chattopadhyay, D., and Sen, M. (2014). Wnt5a-Rac1-NF- κ B homeostatic circuitry sustains innate immune functions in macrophages. *J. Immunol.* **192**, 4386–4397.
- Niibori, Y., Yu, T.-S., Epp, J.R., Akers, K.G., Josselyn, S.A., and Frankland, P.W. (2012). Suppression of adult neurogenesis impairs population coding of similar contexts in hippocampal CA3 region. *Nat. Commun.* **3**, 1253.
- Overk, C.R., and Masliah, E. (2014). Toward a unified therapeutics approach targeting putative amyloid- β oligomer receptors. *Proc. Natl. Acad. Sci. U S A* **111**, 13680–13681.
- Paredes, M.F., Sorrells, S.F., Cebrian-Silla, A., Sandoval, K., Qi, D., Kelley, K.W., James, D., Mayer, S., Chang, J., Auguste, K.I., et al. (2018). Does adult neurogenesis persist in the human hippocampus? *Cell Stem Cell* **23**, 780–781.
- Patrick, E., Rajagopal, S., Wong, H.A., McCabe, C., Xu, J., Tang, A., Imboywa, S.H., Schneider, J.A., Pochet, N., Krichevsky, A.M., et al. (2017). Dissecting the role of non-coding RNAs in the accumulation of amyloid and tau neuropathologies in Alzheimer's disease. *Mol. Neurodegener.* **12**, 51.
- Petersen, R.C., Doody, R., Kurz, A., Mohs, R.C., Morris, J.C., Rabins, P.V., Ritchie, K., Rosser, M., Thal, L., and Winblad, B. (2001). Current concepts in mild cognitive impairment. *Arch. Neurol.* **58**, 1985–1992.
- Picelli, S., Björklund, Å.K., Faridani, O.R., Sagasser, S., Winberg, G., and Sandberg, R. (2013). Smart-seq2 for sensitive full-length transcriptome profiling in single cells. *Nat. Methods* **10**, 1096–1098.
- Pichler, S., Gu, W., Hartl, D., Gasparoni, G., Leidinger, P., Keller, A., Meese, E., Mayhaus, M., Hampel, H., and Riemenschneider, M. (2017). The miRNome of Alzheimer's disease: consistent downregulation of the miR-132/212 cluster. *Neurobiol. Aging* **50**, 167.e1–167.e10.
- Pillat, M.M., Lameu, C., Trujillo, C.A., Glaser, T., Cappellari, A.R., Negraes, P.D., Battastini, A.M.O., Schwindt, T.T., Muotri, A.R., and Ulrich, H. (2016). Bradykinin promotes neuron-generating division of neural progenitor cells through ERK activation. *J. Cell Sci.* **129**, 3437–3448.
- Radde, R., Bolmont, T., Kaeser, S.A., Coomaraswamy, J., Lindau, D., Stoltze, L., Calhoun, M.E., Jäggi, F., Wolburg, H., Gengler, S., et al. (2006). Abeta42-driven cerebral amyloidosis in transgenic mice reveals early and robust pathology. *EMBO Rep.* **7**, 940–946.
- Riascos, D., Nicholas, A., Samaeekia, R., Yukhananov, R., Mesulam, M.-M., Bigio, E.H., Weintraub, S., Guo, L., and Geula, C. (2014). Alterations of Ca²⁺-responsive proteins within cholinergic neurons in aging and Alzheimer's disease. *Neurobiol. Aging* **35**, 1325–1333.
- Rijal Upadhaya, A., Kosterin, I., Kumar, S., von Arnim, C.A.F., Yamaguchi, H., Fändrich, M., Walter, J., and Thal, D.R. (2014). Biochemical stages of amyloid- β peptide aggregation and accumulation in the human brain and their association with symptomatic and pathologically preclinical Alzheimer's disease. *Brain* **137**, 887–903.
- Sahay, A., Scobie, K.N., Hill, A.S., O'Carroll, C.M., Kheirbek, M.A., Burghardt, N.S., Fenton, A.A., Dranovsky, A., and Hen, R. (2011). Increasing adult hippocampal neurogenesis is sufficient to improve pattern separation. *Nature* **472**, 466–470.
- Saito, T., Matsuba, Y., Mihira, N., Takano, J., Nilsson, P., Itoharu, S., Iwata, N., and Saido, T.C. (2014). Single App knock-in mouse models of Alzheimer's disease. *Nat. Neurosci.* **17**, 661–663.
- Salta, E., and De Strooper, B. (2017). microRNA-132: a key noncoding RNA operating in the cellular phase of Alzheimer's disease. *FASEB J.* **31**, 424–433.
- Salta, E., Lau, P., Sala Frigerio, C., Coolen, M., Bally-Cuif, L., and De Strooper, B. (2014). A self-organizing miR-132/Ctbp2 circuit regulates bimodal notch signals and glial progenitor fate choice during spinal cord maturation. *Dev. Cell* **30**, 423–436.
- Salta, E., Sierksma, A., Vanden Eynden, E., and De Strooper, B. (2016). miR-132 loss de-represses ITPKB and aggravates amyloid and TAU pathology in Alzheimer's brain. *EMBO Mol. Med.* **8**, 1005–1018.
- Schindelin, J., Arganda-Carreras, I., Frise, E., Kaynig, V., Longair, M., Pietzsch, T., Preibisch, S., Rueden, C., Saalfeld, S., Schmid, B., et al. (2012). Fiji: an open-source platform for biological-image analysis. *Nat. Methods* **9**, 676–682.
- Serneels, L., Van Biervliet, J., Craessaerts, K., Dejaegere, T., Horr , K., Van Houtvin, T., Esselmann, H., Paul, S., Sch fer, M.K., Berezovska, O., et al. (2009). gamma-Secretase heterogeneity in the Aph1 subunit: relevance for Alzheimer's disease. *Science* **324**, 639–642.
- Shi, Y., Kirwan, P., and Livesey, F.J. (2012). Directed differentiation of human pluripotent stem cells to cerebral cortex neurons and neural networks. *Nat. Protoc.* **7**, 1836–1846.
- Shin, J., Berg, D.A., Zhu, Y., Shin, J.Y., Song, J., Bonaguidi, M.A., Enikolopov, G., Nauen, D.W., Christian, K.M., Ming, G.L., and Song, H. (2015). Single-cell RNA-seq with waterfall reveals molecular cascades underlying adult neurogenesis. *Cell Stem Cell* **17**, 360–372.
- Smith, P.Y., Hernandez-Rapp, J., Jolivet, F., Lecours, C., Bisht, K., Goupil, C., Dorval, V., Parsi, S., Morin, F., Planel, E., et al. (2015). miR-132/212 deficiency impairs tau metabolism and promotes pathological aggregation in vivo. *Hum. Mol. Genet.* **24**, 6721–6735.
- Snyder, J.S. (2019). Recalibrating the relevance of adult neurogenesis. *Trends Neurosci.* **42**, 164–178.

- Sorrells, S.F., Paredes, M.F., Cebrian-Silla, A., Sandoval, K., Qi, D., Kelley, K.W., James, D., Mayer, S., Chang, J., Auguste, K.I., et al. (2018). Human hippocampal neurogenesis drops sharply in children to undetectable levels in adults. *Nature* **555**, 377–381.
- Spalding, K.L., Bergmann, O., Alkass, K., Bernard, S., Salehpour, M., Huttner, H.B., Boström, E., Westerlund, I., Vial, C., Buchholz, B.A., et al. (2013). Dynamics of hippocampal neurogenesis in adult humans. *Cell* **153**, 1219–1227.
- Suh, H., Zhou, Q.-G., Fernandez-Carasa, I., Clemenson, G.D., Jr., Pons-Espinal, M., Ro, E.J., Marti, M., Raya, A., Gage, F.H., and Consiglio, A. (2018). Long-term labeling of hippocampal neural stem cells by a lentiviral vector. *Front. Mol. Neurosci.* **11**, 415.
- Susaki, E.A., Tainaka, K., Perrin, D., Yukinaga, H., Kuno, A., and Ueda, H.R. (2015). Advanced CUBIC protocols for whole-brain and whole-body clearing and imaging. *Nat. Protoc.* **10**, 1709–1727.
- Tartt, A.N., Fulmore, C.A., Liu, Y., Rosoklija, G.B., Dwork, A.J., Arango, V., Hen, R., Mann, J.J., and Boldrini, M. (2018). Considerations for assessing the extent of hippocampal neurogenesis in the adult and aging human brain. *Cell Stem Cell* **23**, 782–783.
- Thal, D.R., Rüb, U., Schultz, C., Sassini, I., Ghebremedhin, E., Del Tredici, K., Braak, E., and Braak, H. (2000). Sequence of Aβ-protein deposition in the human medial temporal lobe. *J. Neuropathol. Exp. Neurol.* **59**, 733–748.
- Theus, M.H., Ricard, J., Bethea, J.R., and Liebl, D.J. (2010). EphB3 limits the expansion of neural progenitor cells in the subventricular zone by regulating p53 during homeostasis and following traumatic brain injury. *Stem Cells* **28**, 1231–1242.
- Tobin, M.K., Musaraca, K., Disouky, A., Shetti, A., Bheri, A., Honer, W.G., Kim, N., Dawe, R.J., Bennett, D.A., Arfanakis, K., and Lazarov, O. (2019). Human hippocampal neurogenesis persists in aged adults and Alzheimer's disease patients. *Cell Stem Cell* **24**, 974–982.e3.
- Toda, T., Parylak, S.L., Linker, S.B., and Gage, F.H. (2019). The role of adult hippocampal neurogenesis in brain health and disease. *Mol. Psychiatry* **24**, 67–87.
- Vadodaria, K.C., Brakebusch, C., Suter, U., and Jessberger, S. (2013). Stage-specific functions of the small Rho GTPases Cdc42 and Rac1 for adult hippocampal neurogenesis. *J. Neurosci.* **33**, 1179–1189.
- van Boxelaere, M., Clements, J., Callaerts, P., D'Hooge, R., and Callaerts-Vegh, Z. (2017). Unpredictable chronic mild stress differentially impairs social and contextual discrimination learning in two inbred mouse strains. *PLoS ONE* **12**, e0188537.
- van Praag, H., Kempermann, G., and Gage, F.H. (1999). Running increases cell proliferation and neurogenesis in the adult mouse dentate gyrus. *Nat. Neurosci.* **2**, 266–270.
- van Praag, H., Schinder, A.F., Christie, B.R., Toni, N., Palmer, T.D., and Gage, F.H. (2002). Functional neurogenesis in the adult hippocampus. *Nature* **415**, 1030–1034.
- Villeda, S.A., Luo, J., Mosher, K.I., Zou, B., Britschgi, M., Bieri, G., Stan, T.M., Fainberg, N., Ding, Z., Eggel, A., et al. (2011). The ageing systemic milieu negatively regulates neurogenesis and cognitive function. *Nature* **477**, 90–94.
- Wang, Y., Veremeyko, T., Wong, A.H.-K., El Fatimy, R., Wei, Z., Cai, W., and Krichevsky, A.M. (2017). Downregulation of miR-132/212 impairs S-nitrosylation balance and induces tau phosphorylation in Alzheimer's disease. *Neurobiol. Aging* **51**, 156–166.
- Wesnes, K.A., Annas, P., Basun, H., Edgar, C., and Blennow, K. (2014). Performance on a pattern separation task by Alzheimer's patients shows possible links between disrupted dentate gyrus activity and apolipoprotein E ε4 status and cerebrospinal fluid amyloid-β42 levels. *Alzheimers Res. Ther.* **6**, 20.
- Wong, H.K.A., Veremeyko, T., Patel, N., Lemere, C.A., Walsh, D.M., Esau, C., Vanderburg, C., and Krichevsky, A.M. (2013). De-repression of FOXO3a death axis by microRNA-132 and -212 causes neuronal apoptosis in Alzheimer's disease. *Hum. Mol. Genet.* **22**, 3077–3092.
- Yang, Y.-T., Wang, C.-L., and Van Aelst, L. (2012). DOCK7 interacts with TACC3 to regulate interkinetic nuclear migration and cortical neurogenesis. *Nat. Neurosci.* **15**, 1201–1210.
- Yassa, M.A., Stark, S.M., Bakker, A., Albert, M.S., Gallagher, M., and Stark, C.E.L. (2010). High-resolution structural and functional MRI of hippocampal CA3 and dentate gyrus in patients with amnesic Mild Cognitive Impairment. *Neuroimage* **51**, 1242–1252.
- Yuniati, L., Scheijen, B., van der Meer, L.T., and van Leeuwen, F.N. (2019). Tumor suppressors BTG1 and BTG2: beyond growth control. *J. Cell. Physiol.* **234**, 5379–5389.
- Zeisel, A., Hochgerner, H., Lönnerberg, P., Johnsson, A., Memic, F., van der Zwan, J., Häring, M., Braun, E., Borm, L.E., La Manno, G., et al. (2018). Molecular architecture of the mouse nervous system. *Cell* **174**, 999–1014.e22.
- Zhao, C., Teng, E.M., Summers, R.G., Jr., Ming, G.L., and Gage, F.H. (2006). Distinct morphological stages of dentate granule neuron maturation in the adult mouse hippocampus. *J. Neurosci.* **26**, 3–11.
- Zhu, Q.B., Unmehopa, U., Bossers, K., Hu, Y.T., Verwer, R., Balesar, R., Zhao, J., Bao, A.M., and Swaab, D. (2016). MicroRNA-132 and early growth response-1 in nucleus basalis of Meynert during the course of Alzheimer's disease. *Brain* **139**, 908–921.

STAR★METHODS

KEY RESOURCES TABLE

REAGENT or RESOURCE	SOURCE	IDENTIFIER
Antibodies		
Anti-BrdU	Abcam	Cat# ab6326; RRID:AB_2313786
Anti-GFP	Abcam	Cat# ab13970; RRID:AB_300798
Anti-Ki-67	Genetex	Cat# GTX16667; RRID:AB_422351
Anti-DCX	Abcam	Cat# ab18723; RRID:AB_732011
Anti-TUBB3	Biologend	Cat# 801202; RRID:AB_10063408
Anti-GFAP	DAKO	Cat# IS524
Anti-PCNA	DAKO	Cat# M0879; RRID:AB_2160651
Anti-IBA1	WAKO	Cat# 019-19741; RRID:AB_839504
Anti-NESTIN	R&D Systems	Cat# MAB1259; RRID:AB_2251304
Anti-SOX2	Santa Cruz	Cat# sc-365823; RRID:AB_10842165
Anti-Cleaved caspase-3	Cell Signaling	Cat# 9661; RRID:AB_2341188
Anti-VG1UT1	Millipore	Cat# AB5905; RRID:AB_2301751
Anti-PSD95	Thermo Scientific	Cat# CP35-100UL; RRID:AB_212825
Anti-mCHERRY	Clontech	Cat# 632496; RRID:AB_10013483
Anti-mCHERRY	LifeSpan	Cat# LS-C204207; RRID:AB_2619713
Virus strains		
Puro:mPGK:mCHERRY lentivirus	Original: Suh et al., 2018 ; Antonella Consiglio, IDIBELL, Barcelona Purchased: VectorBuilder	N/A
CAG:GFP retrovirus	Original: Zhao et al., 2006 ; Rusty Gage Purchased: VectorBuilder	RRID: Addgene_16664
Biological samples		
Human hippocampi	KU Leuven, UZ Leuven, Belgium, Dietmar Thal	N/A
Human blood sera	University of Gothenburg, Sweden, Henrik Zetterberg	N/A
Chemicals, peptides, and recombinant proteins		
Lipofectamine RNAiMAX	ThermoFisher Scientific, Belgium	Cat# 13778075
A β ₁₋₄₂	rPeptide, GA, USA	Cat# A-1163-1
Scrambled A β ₁₋₄₂	rPeptide, GA, USA	Cat# A-1004-1
Critical commercial assays		
miRVana Paris Kit	Life Technologies, Belgium	Cat# AM1556
miRNeasy Micro kit	QIAGEN, Netherlands	Cat# 217084
Superscript II reverse transcriptase	ThermoFisher Scientific, Belgium	Cat# 18064071
miRCURY LNA RT Kit	QIAGEN, Denmark	Cat# 339340
Deposited data		
Single-cell RNA sequencing (FASTQ & metadata)	Gene Expression Omnibus, NCBI	GEO: GSE172402
Experimental models: cell lines		
RenCell VM human NPCs	Millipore, MA, USA	CVCL_E921
Human embryonic stem cells WA09 (H9)	Espuny-Camacho et al., 2013, 2017	RRID:CVCL_9773
Human hippocampal progenitor/stem cell line (HPC0A07/03C)	ReNeuron, UK	RRID:CVCL_9T02

(Continued on next page)

Continued

REAGENT or RESOURCE	SOURCE	IDENTIFIER
Experimental models: mouse strains		
Nestin:GFP	Mignone et al., 2004; Grigori Enikolopov, Stony Brook University, NY, USA	MGI:5523870
APP/PS1 (B6.Cg-Tg(Thy1-APPSw, Thy1-PSEN1*L166P)21Jckr)	Radde et al., 2006; Mathias Jucker, DZNE, Germany	MGI:3765351
App ^{NL-G-F} (App ^{tm3.1Tcs} /App ^{tm3.1Tcs})	Saito et al., 2014; Takaomi Saido, RIKEN Brain Science Institute, Japan	RRID:IMSR_RBRC06344
Oligonucleotides		
miR-132 antagomiR (locked nucleic acid (LNA)-, 3'-cholesterol-modified oligonucleotide)	Exiqon, QIAGEN, Denmark	Cat# 500150; Design ID: 280412
Scramble LNA antagomiR control	Exiqon, QIAGEN, Denmark	Cat# 500150; Design ID: 280407
miR-132 miRIDIAN mimic; UAAC AGUCUACAGCCAUGGUCG (MIMAT0000426)	Dharmacon, Horizon Discovery, Belgium	Cat# C-300599-06
Control miRIDIAN mimic; UCACA ACCUCCUAGAAAGAGUA GA(MIMAT0000039)	Dharmacon, Horizon Discovery, Belgium	Cat# CN-001000-01
Primer mmu-miR-132-3p; UAA CAGUCUACAGCCAUGGUCG	Exiqon, QIAGEN, Denmark	Cat# 204129
Primer mmu-miR-212-3p; UAAC AGUCUCCAGUCACGGCCA	Exiqon, QIAGEN, Denmark	Cat# 206022
Primer mmu-miR-124; UAAG GCACGCGGUGAAUGCC	Exiqon, QIAGEN, Denmark	Cat# 206026
Primers, mRNA (for full sequences, see Table S3)	IDT	Custom primer sets
Software and algorithms		
Fiji	Schindelin et al., 2012	https://fiji.sc/
Imaris x64	Bitplane, Switzerland	https://www.bitplane.com/download/manuals/ReferenceManual6_1_0.pdf
FastQC	FastQC: a quality control tool for high throughput sequence data. Initial contact: Simon Andrews	Version 0.11.5, https://www.bioinformatics.babraham.ac.uk/projects/fastqc/
STAR	Dobin et al., 2013	Version 2.5.2, https://github.com/alexdobin/STAR
Subread/FeatureCounts	Liao et al., 2014	Version 1.5.1
Seurat	Butler et al., 2018	Version 2.3.1, https://satijalab.org/seurat/index.html

RESOURCE AVAILABILITY

Lead contact

Further information and requests for resources and reagents should be directed to and will be fulfilled by the Lead Contact, Evgenia Salta (e.salta@nin.knaw.nl).

Materials availability

This study did not generate new unique reagents.

Data and code availability

The single-cell RNA-sequencing data reported in this paper are available at NCBI Gene Expression Omnibus (<https://www.ncbi.nlm.nih.gov/geo/>) (GEO: GSE172402).

EXPERIMENTAL MODEL AND SUBJECT DETAILS

Animals

Mice were bred according to standard laboratory approaches and housed under standard 12-hour light-dark conditions. The wild-type mice we used were C57BL/6. The AD mouse models used in the study were the *APP/PS1* (MGI:3765351) and *App^{NL-G-F}* (RRID:IMSR_RBRC06344) strains. The first mouse model co-expresses human-mutated APP^{Swe} (KM670/671NL APP) and human mutated presenilin 1 (L166P). These mice [Tg(Thy1-APP^{Sw}, Thy1-PSEN1*L166P) 21Jckr] typically show amyloid deposition in the hippocampus at 3–4 months and cognitive impairment at 7–8 months of age (Radde et al., 2006; Serneels et al., 2009). *App^{NL-G-F}* mice are a more recently established App knock-in model that expresses the APP KM670/671NL (Swedish), APP I716F (Iberian), APP E693G (Arctic) mutations. Similarly to the *APP/PS1* mice, *App^{NL-G-F}* animals develop plaques around the age of 3 months and behavioral deficits from 6 months onward (Saito et al., 2014). For neural stem cell and neuronal progenitor cell visualization *in vivo* and cell isolation from the adult dentate gyrus, the previously characterized Nestin:GFP mice were used (Mignone et al., 2004). For Nestin:GFP⁺-niche cell sorting from the AD dentate gyrus, Nestin:GFP mice (MGI:5523870) were crossed to *App^{NL-G-F}* animals (Nestin-NLGF). All animal experiments were approved by the ethical committees of KU Leuven and UZ Leuven (LA1210596). Health certificates were provided by the Laboratory Animal Center of KU Leuven.

Human samples

The clinical and histopathological information regarding the human hippocampal samples used in the study is summarized in Table S1. Information on collection and processing of the serum samples is provided in Table S4. All experimental procedures with human samples were approved by the ethical committees of KU Leuven, UZ Leuven (S59654) and the University of Gothenburg. Information about medication prescribed to donors has not been disclosed by the respective biobanks, neither has it been employed for data analysis or interpretation.

Human cell lines

RenCell VM human NPCs (Millipore, MA, USA, CVCL_E921) were cultured according to the manufacturer's instructions. Differentiation was induced by withdrawing growth factors (FGF-2 and EGF) from culture media.

Routine culturing and maintenance of human embryonic stem cells (EPSCs) (H9-GFP, RRID:CVCL_9773) (Espuny-Camacho et al., 2013, 2017) was performed using E8-flex growth medium (ThermoFisher Scientific, Belgium). Cells were maintained in a humidified chamber at 37°C with 5% CO₂ and passaged every 4–5 days with 0.5 mM EDTA.

The multipotent human hippocampal progenitor/stem cell line HPC0A07/03C (ReNeuron, UK, RRID:CVCL_9T02), was derived from the first trimester female fetal hippocampal tissue following medical termination and in accordance with UK and USA ethical and legal guidelines, was obtained from Advanced Bioscience Resources (Alameda, CA, USA) and conditionally immortalized by introducing the *c-myc*-ERTAM transgene, which enables cells to proliferate indefinitely in the presence of epidermal growth factor (EGF), basic fibroblast growth factor (bFGF) and 4-hydroxy-tamoxifen (4-OHT). Removal of these factors induces spontaneous differentiation into neurons, astrocytes or oligodendrocytes.

Authentication of all cell lines was provided by the respective original suppliers.

METHOD DETAILS

Intracerebroventricular (i.c.v.) injections

The intracerebroventricular injections were performed as previously described (Jimenez-Mateos et al., 2011) using the following stereotactic coordinates: AP-0.1 mm, ML-1.0 mm, and DV-3.0 mm (from the skull). For miR-132 knockdown, 2 month-old Nestin:GFP or 8 month-old C57BL/6 mice were infused with 2 μ l of miR-132 antagomiR (locked nucleic acid (LNA)-, 3'-cholesterol-modified oligonucleotide) (Exiqon, QIAGEN, Denmark) at 0.33 nmol/ μ l in artificial cerebrospinal fluid (aCSF) (Harvard Apparatus, USA). Control mice received a scrambled LNA oligonucleotide in aCSF. Mice were exposed to voluntary running one week post operation. Analysis of antagomiR-132-injected animals was performed at 3 and 9 months of age, respectively (after 4 weeks of voluntary running). For miR-132 overexpression, 2 month-old Nestin:GFP or 8 month-old *App^{NL-G-F}* and *APP/PS1* mice received either a miR-132 mimic or a negative control oligonucleotide (Dharmacon, Horizon Discovery, Belgium) in a 3 μ l mix with lipofectamine 2000 (at a 1:1 volume ratio) (Thermo Fischer Scientific, Belgium). Injections of 150 pmol oligo each were performed once a week for 5 weeks in total. One week after the first injection, mice were exposed to voluntary running for a total of 4 weeks. Analysis of miR-132 mimic-injected animals was carried out at 9 months of age. Randomization of injectates was employed for all injection sessions, and animals were randomly allocated to each treatment.

Viral vector injections into the dentate gyrus

Male and female 9-month old *App^{NL-G-F}* mice were housed in standard (sedentary) conditions or with a running wheel 1 week prior to surgery. For miR-132 overexpression in adult neural stem cells or progeny, a lentiviral Puro:mPGK:mCHERRY backbone vector (Suh et al., 2018) or a retroviral CAG:GFP (RRID: Addgene_16664) (Zhao et al., 2006) construct were used, respectively, harboring a miR-132 hairpin sequence (VectorBuilder, Germany). Hairpin constructs corresponding to cel-miR-67 were used as negative controls. For stereotactic injections, the viruses were infused (lentivirus: 10⁹ TU/ml; 2 μ l at 0.5 μ l min⁻¹; retrovirus: 10⁸ TU/ml;

5 μl at 0.5 $\mu\text{l min}^{-1}$) into the hemispheric right dentate gyrus (anteroposterior: -2.1 mm from Bregma; mediolateral: 1.9 mm; dorsoventral: 2.2 mm) (van Praag et al., 2002). Mice were kept under sedentary or running conditions and were sacrificed 4 weeks post injection.

Induction of AHN via voluntary running

Mice were housed individually in standard rat cages (45 cm x 20 cm x 20 cm) and divided into sedentary or running groups. Runners had unlimited access to a running wheel in their cage for 30 days. Running distance (km) was monitored electronically (MAFAC, France). No differences in running velocity or distance were observed between wild-type and AD animals.

5-bromo-2'-deoxyuridine (BrdU) injections

BrdU (Sigma-Aldrich, Belgium) was dissolved in 0.9% NaCl at a concentration of 10 mg/ml and was filtered (0.2 μm) under sterile conditions. Mice were pulsed with a single i.p. injection of BrdU (50 mg/kg of body weight) daily for 3 days (at the end of the running period). 24 h after the last BrdU injection they were perfused with 4% paraformaldehyde (PFA) and processed for BrdU immunostaining to identify proliferating neuronal progenitors.

Immunofluorescence in mouse brain sections and cultured cells

For coronal brain sections (16 μm -thick cryosections for VGlut1/PSD95 stainings; 20 μm -thick cryosections for BrdU staining; 40 μm -thick vibratome-prepared sections for Nestin:GFP, Ki-67, DCX staining), tissue was initially permeabilized in 1% (v/v) Triton X-100 (cryosections were first post-fixed in 4% PFA for BrdU and in acetone/methanol for VGlut1/PSD95) and then blocked in 1% (v/v) Triton X-100, 10% (v/v) normal goat serum in PBS for 2 h at room temperature. Primary antibody incubation was carried out in 0.3% (v/v) Triton X-100, 3% (v/v) normal goat serum overnight at 4°C followed by incubation in secondary antibody for 2 h at room temperature. Finally, sections were incubated in DAPI (Sigma-Aldrich, Belgium) and mounted in Mowiol. For immunofluorescent labeling in cells cultured on coverslips, samples were initially permeabilized like before and then incubated in blocking solution (1.5% (v/v) normal donkey serum, 0.2% (v/v) Triton X-100 in PBS) for 1 h at room temperature. Primary and secondary antibody incubation was carried out in blocking solution at 4°C overnight and for 2 h at room temperature, respectively. Finally, cells were stained with DAPI and mounted as described earlier. All the antibodies used for immunolabeling of brain tissue and cultured cells are listed in Table S2.

Immunostaining of human hippocampal sections

An automated staining protocol (Bond Polymer Refine Detection Protocol, Leica Microsystems, Belgium) was followed using a Leica Autostainer (Leica Microsystems, Belgium). Briefly, following dewaxing and rehydration, 5 μm -thick formalin-fixed, paraffin-embedded hippocampal sections were first blocked in 3%–4% (v/v) H_2O_2 and then incubated sequentially with the primary antibody for 30 min, with anti-rabbit poly-HRP IgGs, DAB (3,3'-Diaminobenzidine tetrahydrochloride hydrate) and hematoxylin. In the case of double stainings, the second primary antibody was added to the sections after hematoxylin staining and was followed by incubation in an AP-conjugated antibody and in Bond Polymer Refine Red Detection reagent (Leica Microsystems, Belgium). Finally, the sections were dehydrated and mounted on a Leica automated Coverslipper (Leica Microsystems, Belgium). The antibodies used for immunostaining of human brain samples are listed in Table S2.

Tissue clearing

For brain clearing, the CUBIC protocol (Susaki et al., 2015) was adapted. Briefly, two 1 mm-thick coronal brain sections (Interaural: 1.68/0.88 mm, Bregma: $-2.12/-2.92$ mm) from 4% PFA-perfused brains were initially immersed in 12.5% (w/w) urea, 12.5% (w/w) quadrol and 7.5% (w/w) Triton X-100 for 6 h at 37°C for lipid removal. Subsequently, samples were incubated in 25% (w/w) urea, 25% (w/w) quadrol, and 15% (w/w) Triton X-100 for 24 h at 37°C and the clearing reagent was refreshed after 48 h. The clearing procedure was stopped with washes in 0.01% (w/v) sodium azide in PBS. Refractive index matching was achieved by incubating the sections in 25% (w/w) sucrose, 12.5% (w/w) urea, 5% (w/w) triethanolamine and 0.05% (v/v) Triton X-100 for 24 h at 37°C and then in 50% (w/w) sucrose, 25% (w/w) urea, 10% (w/w) triethanolamine and 0.1% (v/v) Triton X-100 for 48 h with refreshing the solution every 24 h.

Fluorescence *in situ* hybridization (FISH)

40 μm -thick vibratome coronal brain sections were post-fixed in 4% PFA for 15 min and then acetylated in a hydrochloric acid, triethylamine, acetic anhydride solution for 1 min in the dark. Following prehybridization in hybridization buffer (50% formamide, 5x saline-sodium citrate (SSC), 500 $\mu\text{g/ml}$ yeast t-RNA, 1x Denhardt's solution) at 60°C for 1 h, samples were hybridized with 42 nM of miR-132 or scramble probe (Ribotask, Denmark) at 70°C overnight. After sequential washes in 0.2x, 0.5x, 2x SSC buffer and brief incubation in 3% H_2O_2 , blocking was performed in 0.5% Blocking Reagent (blocking solution) (Roche Diagnostics, Belgium) for 1 h at room temperature. Finally, sections were probed with an anti-fluorescein HRP-conjugated antibody (Roche Diagnostics, Belgium) in blocking solution for 1 h and signals were developed in TSA Plus Fluorescein reagent (Perkin Elmer, USA). For subsequent immunofluorescent labeling, the sections were processed as described earlier.

Image acquisition, processing and analysis

For the PCNA staining in human samples, one hippocampal section per case was screened using a widefield Zeiss Axioplan 2 (Zeiss, Belgium). PCNA⁺-nuclei at the subgranular layer of the dentate gyrus within an area that included in total 1000 hematoxylin-stained

nuclei were encountered for quantification. Cells with cytoplasmic PCNA⁺-signal were excluded from the analysis, as these may include IBA⁺-proliferating microglia (see [Figures S1A–S1F](#)). The average of the cell counts in the non-demented control cohort was used for the normalization of all the samples.

For immunolabelled mouse brain sections and cultured cells, images (z-stacks) were acquired using a Nikon A1R Eclipse Ti confocal microscope (Nikon, Belgium), unless differently stated. The FIJI software ([Schindelin et al., 2012](#)) was employed for image processing and quantification. For multi-channel confocal images, distinct channels were overlaid using the 'Merge Channel' function in FIJI (overlaid images are indicated as 'Merge' in figures). For BrdU immunostaining in cryosections, three sections per sample were used with 200 μm distance between each two sections. The number of BrdU⁺-cells in the subgranular zone of the dentate gyrus was normalized to the total length of the dentate for each section (BrdU⁺-cells divided by dentate gyrus length). Average values for each sample were calculated by averaging the normalized values of the three sections per sample. For Nestin:GFP, Ki-67 and DCX immunostaining in vibratome-prepared sections, 9–12 sections (with 40 μm distance between each two sections) per sample were used for quantification. Ki-67⁺- (in all the samples) and DCX⁺- (only in the *APP/PS1* and *App^{NL-G-F}* dentate gyrus) cells were manually counted per section and average values per sample were calculated by averaging the values of all sections of the same sample. In Nestin:GFP- and DCX- (only in the Nestin:GFP dentate gyrus) immunostained samples, due to the strong signal, the mean intensity values instead of the cell counts were used. Similarly to before, 9–12 sections (with 40 μm distance between each two sections) per sample were used for quantification. Average values per sample were calculated by averaging the values of all sections of the same sample and the values of the control-injected sedentary animals were used for the normalization of all the samples.

For image acquisition of the cleared brain sections, a CSU-X1 spinning disk confocal microscope (tile-scan/z stack, 10x plan fluor NA 0.3, 488nm laser line) (Nikon, Belgium) was used and 3D rendering of z stacks was carried using Imaris x64 software (Bitplane, Switzerland). Briefly, GFP⁺-cells were automatically identified as 10 μm 'spots' based on size and intensity thresholds were evenly applied for all samples. Reconstructed surfaces were volume-filtered to exclude those not belonging to the dentate gyrus. Spots up to 10 μm close to the dentate gyrus surface were considered for quantification. Values were normalized against the average of the scramble-injected group.

Video files were prepared in Imaris at a 360° angle and at 200 frames of horizontal movement, and saved at 24.000 frames per second and at 640 × 480 VGA.

For quantification of colocalized pre/post-synaptic puncta, images acquired with a 40x oil lens were subjected to deconvolution and maximum intensity projections of z series were created with the Imaris x64 software. Dots were filtered by size (0.1–0.93 μm^3) and the number of contact sites and the size of the analyzed area were calculated per image.

For assessing dendritic arborization, images of mCHERRY⁺- and GFP⁺- cells were acquired by regular confocal microscopy in vibratome-prepared sections. Branching points were counted manually, while the FIJI software was used for quantification of total dendritic length in the same cell. For assessing spine density, dendritic images of mCHERRY-labeled cells were acquired using the Zeiss LSM880 Airyscan super-resolution system (Carl Zeiss, Belgium), while dendritic images of GFP-labeled cells were obtained with a Leica TCS SP8 X microscope (Leica Microsystems, the Netherlands). More specifically, images of labeled dendritic processes at the outer molecular layer were acquired at 0.2 μm intervals with a 63x oil lens and a digital zoom of 2 (Zeiss LSM880 Airyscan) or at 0.1 μm intervals with a 40x oil lens and a digital zoom of 6 (Leica TCS SP8 X). Images were subjected to deconvolution and maximum intensity projections of z series were created with the Imaris x64 software. The length of each dendritic segment was determined by tracing the center of the dendritic shaft and the number of spines was counted automatically from the two-dimensional projections. The linear spine density was calculated by dividing the total number of spines by the length of the dendritic segment.

RenCell transfections

For RenCell transfections, 40%–60% confluent cultures were transfected with miR-132 mimic and control oligonucleotides (at 0.1 pmol or 0.01pmol, depending on the experimental conditions, Dharmacon, Horizon Discovery, UK) or miR-132 antisense inhibitor and control oligonucleotides (at 50 pmol, Dharmacon, Horizon Discovery, UK) using lipofectamine RNAiMAX (ThermoFisher Scientific, Belgium) according to the manufacturer's instructions. Cells were collected for RNA extraction or fixed for immunostaining three days post transfection. For miR-132 inhibition experiments, differentiation was induced 24 h post transfection.

Neural induction of human embryonic pluripotent stem cells

Neural induction of human pluripotent stem cells (NPCs) was carried out according to a previously published protocol ([Shi et al., 2012](#)) with some modifications. Briefly, on DIV (days *in vitro*) –2 of neural induction, cells were enzymatically dissociated with StemPro Accutase cell dissociation reagent (Biolegend, CA, USA) and single cells were plated (1.5×10^6 /well) in Matrigel-coated (Corning, Sigma-Aldrich, Belgium) 6-well plates in mTeSR1 growth medium (STEMCELL Technologies, France) supplemented with 10 mM Y-27632 ROCK inhibitor (Calbiochem, CA, USA). On DIV0, for initiation of neural induction, the culture medium was replaced with neural maintenance medium supplemented with 1 μM StemMACS LDN-193189 (Miltenyi, Biotec, Netherlands) and 10 μM SB431542 (STEMCELL Technologies, France). Neural induction was carried out for 12 days with daily replacement of growth media. After the neural induction, neuroepithelium was passaged three times using Dispase-II (Roche, Belgium) to enrich for neural rosettes. Culture medium was supplemented with 20 ng/ml FGF (PeproTech, Belgium) during the first Dispase-II step for expansion. Around DIV29, neural rosettes were dissociated using the StemPro Accutase cell dissociation reagent and plated on laminin-coated culture dishes in neural maintenance medium for further maturation. RNA samples were collected on day DIV-2 (PSCs), day DIV29 (NPCs) and DIV60 (neurons).

Preparation of A β ₁₋₄₂ oligomers and neuronal precursor cell treatment

Oligomerization and characterization of A β ₁₋₄₂ was carried out as previously described (Brkic et al., 2015; Kuperstein et al., 2010). Briefly, A β ₁₋₄₂ (A-1163-1, rPeptide, GA, USA) or scrambled A β ₁₋₄₂ (A-1004-1, rPeptide, GA, USA) were dissolved at a concentration of 1 mg ml⁻¹ in hexafluoroisopropanol (HFIP, Sigma-Aldrich, Belgium). A gentle stream of nitrogen gas was used to evaporate HFIP. The resulting pellet was resuspended in DMSO, and buffer was exchanged with Tris-EDTA using a 5 ml HiTrap desalting column (GE Healthcare, Belgium) according to the manufacturer's instructions. Determination of the eluted peptide concentration was performed using the Bradford method (Bio-Rad, Belgium). The eluted peptide was allowed to aggregate for 2 h at room temperature. EPSC-derived human neuronal precursor cells were incubated in neural maintenance medium containing 5 μ M A β ₁₋₄₂ or scramble control peptide for 72 h. Six biological replicates per treatment were used.

Treatment of human neuronal precursor cells with AD and control serum

Serum incubation of human neuronal precursors (HPC0A07/03C) was performed as previously described (Maruszak et al., 2017). 24 h after seeding, proliferation medium containing EGF, bFGF and 4-OHT was replaced with proliferation medium additionally supplemented with 1% serum. Serum information can be found in Table S4. After 48 h of proliferation, differentiation was induced by replacing culture medium with medium supplemented with 1% serum but devoid of EGF, bFGF and 4-OHT. Each serum treatment was performed in triplicates. Samples were collected for RNA isolation after 7 days of differentiation.

RNA isolation, reverse transcription and real-time PCR

The dentate gyrus from adult mouse brain was microdissected as previously described (Hagihara et al., 2009). RNA extraction from whole dentate gyri was performed using the miRVana Paris Kit (Life Technologies, Belgium) according to the manufacturer's instructions. Briefly, tissue was homogenized in 350 μ l cell disruption buffer supplemented with protease and phosphatase inhibitors. Following denaturation, addition of acid phenol:chloroform, incubation, and centrifugation, 1.25 volumes of ethanol 100% were added to the aqueous phase. The samples were then loaded on miRVana spin columns and processed according to the manufacturer's instructions. For isolating RNA from cultured cells, cells were first collected in 1 ml Trizol (Thermo Fisher Scientific, Belgium). Following incubation in chloroform and centrifugation 1.25 volumes of ethanol 100% were added to the aqueous phase and the samples were loaded and processed on miRVana spin columns like before. FACsorted cells were initially collected in RNaprotect Cell reagent (QIAGEN, Netherlands) and following brief centrifugation, cell pellets were processed using the miRNeasy Micro kit (QIAGEN, Netherlands) according to the manufacturer's instructions. Reverse transcription of 200 ng (mRNA) or 100 ng (miRNA) RNA was performed using the Superscript II reverse transcriptase (ThermoFisher Scientific, Belgium) for protein-coding transcripts and the miRCURY LNA RT Kit (Exiqon, QIAGEN, Denmark) for miRNAs. Real-time semi-quantitative PCR was performed using the SensiFast Sybr No-Rox kit (Bioline, UK) for coding transcripts and the Sybr Green mastermix and LNA PCR primers (Exiqon, QIAGEN, Denmark) for miRNAs. Mean expression of two housekeeping genes was used for all normalizations (U6 snRNA, RNU5G for miRNAs, *Actb* and *Gapdh* for murine mRNAs, and *18S* and *GAPDH* for human mRNAs). The primer sequences can be found in Table S3. Cp (crossing points) were determined by using the second derivative method. Fold changes were calculated with the $\Delta\Delta$ Ct method (Livak and Schmittgen, 2001).

Adult dentate gyrus dissociation for fluorescence activated cell sorting (FACS) of Nestin:GFP⁺ cells

Dentate gyri (each sample consisted of 1 full dentate gyrus; right and left hemisphere) were first dissected and minced in Hibernate A Low Fluorescence (BrainBits, IL, USA) on ice. Tissue dissection was carried out in 20U/ml papain and 50U/ml DNaseI (Worthington, NJ, USA) for 20 min at 37°C. The enzymatic digestion was stopped by incubating the samples in 10 mg/ml ovomucoid solution (Worthington, NJ, USA), cells were dissociated by trituration, filtered through a 70 μ m nylon mesh, span down and eventually resuspended in ice-cold Hibernate A. Debris and myelin removal was performed using the adult brain dissociation kit (Miltenyi Biotec, Netherlands) according to the manufacturer's instructions. Finally, cells were resuspended in ice-cold Hibernate A and dead cells were stained with propidium iodide (ThermoFisher Scientific, Belgium). GFP⁺- and GFP⁻-cells were sorted in a FACS Aria III (BD Biosciences, CA, USA) in RNase-free eppendorfs (in bulk) or in 96-well plates (in single) for downstream analysis.

Behavioral testing

For contextual fear conditioning assessment, a passive avoidance protocol was employed using a two (an illuminated and a dark one, separated by a guillotine door)-compartment box with a shock grid (Callaerts-Vegh et al., 2015; D'Hooge et al., 2005). Briefly, dark-adapted, single-housed 9-month old male mice were placed in the illuminated box and latency to enter the dark compartment was recorded. Upon entry into the dark compartment (all four paws inside), the door was closed and a 2 s foot shock (0.2 mA) was applied. The mice were then immediately removed from the box and placed back in their home cage. Twenty four hours later, the dark-adapted mice were again placed in the illuminated box and latency to enter the dark compartment was measured as retention of contextual memory. A maximum of 300 s was noted in case the animal would not enter within the first five minutes.

Pattern separation in 9-month old male mice was measured using an adapted fear conditioning protocol (van Boxelaere et al., 2017; Nakashiba et al., 2012). Briefly, animals were fear conditioned in a specific context (A) by placing them in a conditioning cage (25 \times 25 \times 25 cm) fitted with stainless steel grid floors to deliver mild foot shocks and located in sound-attenuating cubicles (Panlab Startle & Fear Combined System (Panlab, Spain)). Animal movement was monitored by a motion-sensitive floor (the degree of motion could range from 0 to 100) connected to an interfaced computer using Panlab Freezing v1.2.0 software.

Freezing was counted if registered movement remained below the arbitrarily defined threshold of 2.5 for at least 1 s. Before testing, animals were placed in a holding area for 30 min for habituation. Contextual fear conditioning consisted of 3 days conditioning in context A, followed by 2 days context testing (A, B, and C, see [Figure 7B](#)). In contextual fear acquisition (Days 1–3), mice were placed in context A and after 3 min exploration, a foot shock (2 s; 0.5 mA) was delivered. One minute later, mice were removed from the testing box and placed in their housing cage. Freezing was measured during the 3 min interval preceding the shock.

To determine the specificity of contextual fear conditioning, freezing behavior in contexts A, B and C was recorded during the generalization testing (Days 4–5). On day 4, mice were placed in context A without shocks for 3 min, then removed and placed in a housing cage. 120–150 min later, mice were placed in context B (same features as A, except for an inserted A-frame roof made of black cardboard) and, eventually following the same procedure as before, in context C (change in tactile, olfactory and visual dimension). The testing order between the four groups was randomized to minimize testing time effect, but all animals were tested first in one context before the next context was presented. On day 5, the same procedure was followed but the order of context presentation was changed to B → A → C. Freezing was measured during a 3 min interval and freezing behavior in a similar (B) or a different (C) context was recorded as a measure of discrimination learning (pattern separation).

Temozolomide (TMZ) treatment

TMZ (Sigma-Aldrich, Belgium) solution (in 10% DMSO) was diluted in 0.9% NaCl to a concentration of 2.5 mg/ml. Control vehicle solution was similarly prepared using 10% DMSO in 0.9% NaCl without TMZ. TMZ or control vehicle were administered i.p. at a dose of 12.5 mg/kg of body weight once a day for 3 consecutive days, followed by 4 days of no injections (one cycle). i.c.v. injections of miR-132 or control mimic were every time performed 2 days after the last TMZ or control vehicle injection of each cycle. After 4 cycles, mice were subjected to the avoidance test.

Smart-seq2 processing and single-cell library preparation

For FACS isolation of single cells, four miR-132-injected and four control-injected Nestin:GFP male mice were used and 94 cells were initially sorted per mouse. FACS-sorted cells were processed using the Smart-seq2 protocol ([Picelli et al., 2013](#)). Briefly, RNA was reverse-transcribed using biotinylated oligo-dT primers (IDT DNA, Belgium) and biotinylated template-switching (TSO) oligonucleotides (Exiqon, QIAGEN, Denmark) and subsequently cDNA was preamplified using the KAPA HiFi Hot Start DNA Polymerase (KAPA Biosystems, Roche Diagnostics, Belgium) and biotinylated ISPCR primers (IDT DNA, Belgium). cDNA was purified using AMPURE XP Agencourt beads (Beckman Coulter, France), concentration was calculated with the Quantifluor dsDNA kit (Promega, Netherlands) and adjusted on an Echo 525 Liquid Handler (Labcyte, CA, USA). 100 pg cDNA per cell were used for library preparation with Nextera XT DNA Library Preparation Kit (Illumina, CA, USA). Finally, following purification on magnetic beads the libraries were multiplexed and sequenced using the Illumina NextSeq500 platform (Illumina, CA, USA).

Data processing

To confirm quality of the raw reads, a FastQC analysis (Version 0.11.5, <https://www.bioinformatics.babraham.ac.uk/projects/fastqc/>) was performed. Reads were aligned to the mouse mm10 genome (Ensembl Version 88) using STAR (Version 2.5.2 ([Dobin et al., 2013](#))) with default options. A count table was generated from the alignments using Subread/FeatureCounts 1.5.1 ([Liao et al., 2014](#)).

The count matrix was analyzed with Seurat 2.3.1 ([Butler et al., 2018](#)), using the following workflow: Cells with less than 200 genes or more than 6,000 genes (likely doublets) were removed, as well as cells whose mitochondrial gene expression accounted for more than 20% of the total gene expression of that cell. Genes found in less than 0.5% of cells were also excluded. Following this filtering, 709 of the original 768 cells remained (with a median read depth of 630,131 reads per cell and median of 2,646 genes per cell). Data were log-normalized and scaled by a factor of 10,000. The normalized count data were subsequently regressed on the number of reads. Principal component analysis (PCA) was performed using the top 1,438 highly variable genes. The first 30 PCAs were used to identify clusters (using default parameters). Data was visualized using t-Distributed Stochastic Neighbor Embedding (t-SNE). Cluster markers were determined by a differential expression analysis of each cluster versus all other clusters combined ([Table S5](#), ClusterMarkers). Seurat's "AddModuleScore" function, with default parameters, was used to calculate gene set scores of cell-type-specific markers extracted from previous studies ([Table S5](#), LiteratureMarkers) ([Artegiani et al., 2017](#); [Hochgerner et al., 2018](#); [Zeisel et al., 2018](#)). Boxplots of these scores were used to assign each cluster to a cell type (for summary data see [Table S5](#), ModuleScore). We confirmed these assignments by comparing our cluster markers to unique markers of cell type defined by the aforementioned studies to ensure that there was no ambiguity in the assignment of cell types. Gene differential expression between experimental (miR-132 overexpression) and control conditions (within each cell population) was performed ([Table S6](#)). Differential expression (for analysis of cluster markers and for analysis between controls and experimental conditions) was performed as follows: p values were calculated using a Wilcoxon rank-sum test (using Seurat's "FindMarkers" function), and corrected for multiple testing using a Bonferroni correction. Log fold changes were calculated using the natural logarithm. Genes with adjusted p values of < 0.05 were considered significantly differentially expressed. All sequencing data reported in this study are available at the NCBI Gene Expression Omnibus (GEO Accession Number: GSE172402).

Functional enrichment analysis was performed by using Ingenuity Pathway Analysis (IPA, Ingenuity Systems Inc., Redwood City, CA, USA). By convention, the 150 transcripts with the most negative ('Downregulated Transcripts', left side of x axis) or most positive

('Upregulated Transcripts', right side of x axis) log fold changes after differential gene expression (comparing miR-132-overexpression to control samples) were selected per cluster for analysis.

QUANTIFICATION AND STATISTICAL ANALYSIS

Statistical analyses were every time performed as indicated in the pertinent figure legend. For all experiments, at least three biological or experimental replicates were analyzed. Sample size for each experiment is indicated in the corresponding figure legend. Unless otherwise specified, statistical analyses of non-RNA-seq data were performed using GraphPad Prism and differences were considered significant at p value < 0.05. Specific p values are indicated in the figures. For the analysis and quantification workflow of imaging data please refer to STAR Methods, 'Image acquisition, processing and analysis'. For the single-cell RNA-seq experiment, 4 mice per group were used to obtain adequate cell numbers for one replicate. Statistical analyses of the single-cell RNA-seq data are described in STAR Methods, 'Data processing'. Randomization of mice from different experimental groups was deployed for all the stereotactic injections and behavioral testing. Analysis and quantification of imaging data (from both human and mouse brain) and behavioral experiments in mice (oligonucleotide injections, testing and data analysis) were performed in blind. No inclusion or exclusion criteria of data or subjects were applied in non-RNA-seq experiments. Filtering in RNA-seq analysis was applied as indicated under 'Data processing'.